UNIVERSITÁ DEL SALENTO

Facoltá di Scienze Matematiche, Fisiche e Naturali
Dipartimento di FISICA

Dottorato di Ricerca in Fisica
XIX Ciclo

Ph.D. Thesis
Settore Scientifico Disciplinare FIS05

Laboratory study of dust for remote sensing applications

Tutor: Prof. Sergio Fonti

Candidate: Romolo Politi

Anno Accademico 2006-2007

"... Non vogliate negar l'esperienza
di retro al sol, del mondo sanza gente.
Considerate la vostra semenza
fatti non foste a viver come bruti
ma per seguir virtute e canoscenza"
Dante Alighieri, Divina Commedia,
Inferno, Canto XXVI 116-120

Contents

Introduction

The aim of this work is to analyze the importance of the correct determination of the grain size of particles in laboratory spectroscopy and, in particular, I emphasize the effect of an uncorrected diameter determination in some applications aimed to the interpretation of remote sensing data. I shall therefore describe the parametrization of the sample, from a chemical and morphological point of view. I widely discuss, also, the measurement technique and the application of Hapke theory to reflectance spectra of intimate mixtures, examining in particular the influence of the particles diameter (including the correlated parameters) on theoretical prediction.

In the first chapter, I shall briefly describe the Martian research scenario, focusing on the results of the last space missions. I shall then introduce, the radiative transfer equation as starting point for the description of Hapke theory of reflectance.

In the second chapter I shall discuss the procedure used for the production of the samples, from the bulk piece to the fine particulate, and the problems linked to the determination of the actual grain size using laser diffractometry. I shall also describe a procedure aimed to obtaining a good gaussian fit for the grain size distribution and discuss some parameters that could by useful in assuming the reliability of the

description of dimensional distribution.

In the third chapter I shall describe the theory of the intimate mixture using Hapke's equations of reflectance. I shall present some examples in while the different index of dimensional purity, to emphasize the role of grain size in the intimate mixtures. I shall also describe chemical, physical and optical properties of the minerals used in laboratory simulations and chosen according to the suggestion of remote sensing results.

In the fourth and last chapter I shall discuss the importance of optical constants in planetary research, in particular when a radiative transfer model is used for the comparison with the observed spectra. At the same time, the methodology for the derivation of the optical constants from reflectance measurements will be illustrated as a natural consequence of the theory developed in the previous chapters.

Chapter 1

Interaction Radiation-Matter

This chapter describes the status of art of Martian surface exploration and the methodologies for its study. In particulary I shall describe interaction radiation-matter used for planetary purpose, essentially as an introduction to the theory of reflectance, dealt with in the following chapter.

1.1 Martian surface

The search for signs of the stable presence of liquid water on the Martian surface in the past and also at present is an extremely important issue which can give precious information about the geological and climatological evolution of Mars and could have very important implications on the possibility that life developed at some stage on the planet (McKay & Stoker, 1989; McKay *et al.* , 1996). Today the temperature and the atmospheric pressure on the surface of Mars are low enough

to prevent the stable presence of liquid water which usually freezes solid and then quite rapidly sublimates, except in the polar regions where ice is relatively stable. However, climatic models (Pollack *et al.* , 1987; Forget & Pierrehumbert, 1997; Yung *et al.* , 1997) suggest the possibility that, in the past, Mars may have experienced episodes of warmer and wetter climate with a thicker atmosphere able to provide a strong greenhouse effect and to stabilize liquid water on the Martian surface. This hypothesis is supported by remote sensing images which show the presence of sinuous and dendritic channels, apparently carved through slow erosion by water flowing across the surface (Masursky *et al.* , 1977; Malin & Carr, 1999; Williams & Phillips, 2001), along with paleolacustrine basins which could have hosted relatively large bodies of liquid water for a significant period of time (Goldspiel & Squyres, 1991; Cabrol & Grin, 1999).

In this scenario evaporites, such as carbonates, sulfates and other salts, could therefore play a crucial role. The presence of massive evaporite deposits on the Martian surface could strongly indicate that bodies of liquid water existed in the past on the Martian surface for a sufficiently long period of time and imply an ancient climate much warmer and wetter than the current one. In this framework our group has previously focused its attention on the spectral properties of carbonates and sulfates by means of a series of laboratory and theoretical works (Orofino *et al.* , 1998; Orofino *et al.* , 2000, 2002; Fonti *et al.* , 2001; Marzo *et al.* , 2004). However, apart from the identification of small quantities of carbonates in the Martian dust (Bandfield *et al.* , 2003; Lellouch *et al.* , 2000; Pollack *et al.* , 1990), no carbonate deposits have been found so far on Mars (Christensen *et al.* , 1998; Bibring *et al.* , 2005; Burns, 1970). On the other hand, magnesium and calcium sulfates have been identified by the spectrometer OMEGA (Observatoire pour la Minéralogie, l'Eau la

Glace et l'Activité) onboard the Mars Express spacecraft in various small areas of the planet (Bibring *et al.* , 2005). In spite of the limited extension of these deposits, this discovery could be very important since the Martian sulfates could be present within a much more extended subsurface layer, appearing at the surface only in the few places detected by OMEGA.

Another way to search for the ancient presence of liquid water on the Martian surface is to find in the observed spectra the characteristic bands of aqueous alteration of the superficial minerals. Indeed the interaction of liquid water with the minerals present on the surface alters, in principle, the chemical and physical properties of such minerals and this alteration can be detected by remote sensing spectroscopic observations. Among the materials of Martian interest, olivine is particularly important since it readily alters to iddingsite and various phyllosilicate minerals in the presence of water (Colman, 1986). For this reason the discovery of massive outcrops of this mineral on the surface of Mars could give extremely important information on the climate history of the planet. In fact, if large quantities of pristine olivine were present in very ancient regions of Mars, this would imply that chemical erosion by water was low on the planet and that Mars has been cold and dry throughout most of its geologic history. On the contrary the presence of massive quantities of altered olivine, or of the final products of olivine alteration, should indicate that in the past the Martian climate was wetter and warmer enough to allow the stability of liquid water on the surface of the planet. At present, however, apart from the tentative identification of olivine on the surface (Christensen *et al.* , 2000) and in the atmospheric dust (Grassi & Formisano, 2000), the spectroscopic evidence for the presence of large quantities of olivine on the Martian surface are still lacking. Hoefen *et al.* (2003) have recently identified olivine with different iron

content in the spectra of various Martian areas taken by the Thermal Emission Spectrometer (TES) onboard the Mars Global Surveyor spacecraft. This work has shown, however, that olivine-rich areas found so far cover only a very small percentage of the Martian surface between 60° N and 60° S, with the largest outcrop occurring in Nili Fossae (northeastern Syrtis Major). OMEGA also found olivine in a few specific areas of the Martian surface (Bibring *et al.* , 2005; Mustard *et al.* , 2005b); in addition, very interestingly, OMEGA spectra have shown that in Nili Fossae as well as in the Mawrth Valles region, the olivine deposits are associated with outcrops enriched in phillosilicates, likely Fe-rich smectite clays (Poulet *et al.* , 2005; Mustard *et al.* , 2005a). This relation between phyllosilicate- and olivine-rich areas rises the possibility that the presence of unaltered olivine can be due to a recent exposure of ancient buried deposits rather than a lack of aqueous alteration and suggests a geologically long period of weathering in the early history of Mars (Poulet *et al.* , 2005). However the discovery of phyllosilicate-rich regions is too recent to draw definite conclusions about the climatic evolution of the Red Planet.

1.2 Equation of radiative transfer

The formalism commonly used to describe how the intensity of an electromagnet wave is changed by the process of emission, absorbtion, and scattering, as the wave propagates through a complex medium, is a form of the transport equation known as the *equation of radiative transfer*. The fundamental assumption of this formalism is that the inhomogeneities of the medium emit and scatter the radiation independently of each other and incoherently. This is the case when the material consist of discrete molecules or particles that are randomly positioned and oriented. Thus, with care,

the theory is applicable to the two media that are of greatest interest in remote sensing: atmospheres and regoliths. However, it will not give correct results if the particles are not uniformly spaced and regular in shape.

We consider a radiance field $I(s, \Omega)$[1], which describes the electromagnetic radiation at point s, propagating in the direction Ω, that has been emitted or scattered at least once within a particulate medium. Suppose s lies on the base of a right cylinder of area dA, length ds, and volume $dsdA$, where ds points in direction of Ω, as shown in figure 1.1. The radiant energy at s, passing through the base of the cylinder and

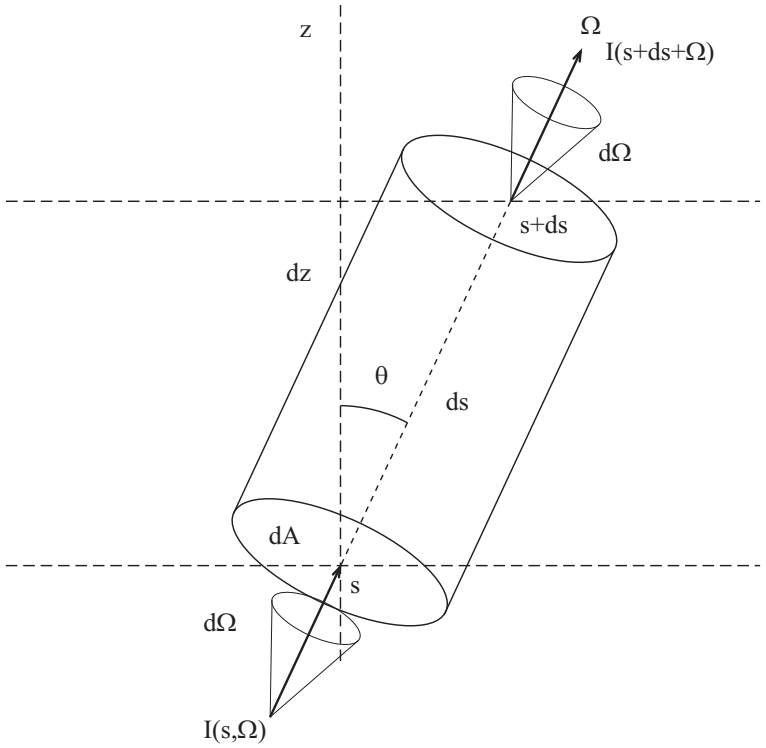

Figure 1.1: Geometry used for the derivation of radiative transfer equation.

contained in a cone of solid angle $d\Omega$ about Ω is $I(s, \Omega)dAd\Omega$. Similarly, the power

[1]In general $I(s, \Omega)$ would be also function of the wavelength or frequenciy, however, in the interest of the economy of notation this dependence will not be denoted explicitly.

emerging from the top of the cylindrical volume into $d\Omega$ is

$$I(s+ds,\Omega)dAd\Omega = \left[I(s,\Omega) + \frac{\partial I(s,\Omega)}{\partial s}ds\right] dAd\Omega. \tag{1.1}$$

The difference between the power emerging from the top and that entering at the bottom is $(\partial I/\partial s)dsdAd\Omega$. More generally, $\partial I/\partial s$ is the divergence of I in the direction of Ω,

$$\frac{\partial I}{\partial s} = \Omega \cdot \operatorname{div} I \tag{1.2}$$

The change in radiant power is due to various processes occurring in the cylinder that add or subtract energy from the beam. We will be basically concerned with three of such process: absorption, scattering, and emission. The effects of absorption and scattering that subtract energy from the radiance are usually grouped together into a single process called *extinction*. The *volume extinction coefficient*, $E(s,\Omega)$, of the medium is defined such that the decrease in power ΔP_E due to extinction as the beam propagates through the volume element is

$$\Delta P_E = -E(s,\Delta\Omega)I(s,\Delta\Omega)dsdAd\Omega. \tag{1.3}$$

If extinction were the only process acting on the intensity, then

$$\Delta P_E = \frac{\partial I}{\partial s}dsdAd\Omega = dIdAd\Omega, \tag{1.4}$$

and the fractional change in the average intensity would be

$$dI/I = -Eds, \tag{1.5}$$

which may be integrated to

$$I(s) = I(0) \exp\left[-\int_0^s E(s')ds'\right]. \tag{1.6}$$

The volume extinction coefficient may be separated into the *volume absorption coefficient*, $K(s, \Omega)$, and the *volume scattering coefficient*, $S(s, \Omega)$, where

$$E(s, \Omega) = K(s, \Omega) + S(s, \Omega) \tag{1.7}$$

In a similar way we could define the decrease of power due to the scattering as

$$\Delta P_S = \frac{1}{4\pi} G(s, \Omega, \Omega') I(s, \Omega') ds dA d\Omega' d\Omega \tag{1.8}$$

that describes the decrease of the intensity $I(s, \Omega')$ propagating through the volume $dsdA$ in a direction Ω' and scattered into the direction Ω, weighed by the *volume angular scattering coefficient*, $G(s, \Omega, \Omega')$.

To find the total amount of power ΔP_S scattered into the beam through the volume the contributions coming from all the directions Ω' must be added together, so that

$$\Delta P_S = \int_{4\pi} dP_S d\Omega' = ds dA d\Omega \frac{1}{4\pi} \int_{4\pi} I(s, \Omega') G(s, \Omega, \Omega') d\Omega' \tag{1.9}$$

The integral of $G/4\pi$ over all directions is the volume scattering coefficient,

$$S(s, \Omega) = \frac{1}{4\pi} \int_{4\pi} G(s, \Omega, \Omega') d\Omega'. \tag{1.10}$$

For an ensemble of randomly oriented particles, G depends only on the scattering angle θ' between Ω' and Ω, rather then on the two direction separately. In this case,

S is independent of Ω, and $d\Omega' = 2\pi \sin\theta' d\theta'$, so that

$$S(s) = \frac{1}{2}\int_0^\pi G(s,\theta')\sin\theta' d\theta'. \tag{1.11}$$

Let the *volume emission coefficient* $F(s,\Omega)$ be the power emitted per unit volume by the element at position s into unit solid angle about the direction Ω. Then $F(s,\Omega)$ is defined so that the contribution of the emitted radiation to the change of power is

$$\Delta P_F = F(s,\Omega) ds dA d\Omega. \tag{1.12}$$

In general, there are at least four process that may contribute to the volume emission: single scattering, thermal emission, fluorescence[2] and luminescence[3], and stimulated emission. Fluorescence and luminescence will not considered in this discussion. Stimulated emission is important in gaseous media that are not in thermodynamic equilibrium, but usually not in particulate media. Hence, only single scattering and thermal emission will be considerate; their volume coefficients will be denoted by $F_S(s,\Omega)$ and $F_T(s,\Omega)$ respectively. Then

$$F(s,\Omega) = F_S(s,\Omega) + F_T(s,\Omega) \tag{1.13}$$

[2]The fluorescence is the slow emission of longer wavelength light following the absorption of shorter wavelength radiation. Fluorescence is common with aromatic compounds with several rings joined together. Phosphorescence is similar but may persist long after the stimulating radiation is extinguished.

[3]The luminescence is the visible light produced from a surface submitted to invisible radiation such as UV, X rays and son on. Unlike fluorescent light it continues to be emitted after the existing source is removed, gradually fading away.

Equating the sum of all the contributions $(\Delta P_S + \Delta P_E + \Delta P_F)$ to $(\partial I/\partial s)dsdAd\Omega$ gives

$$\frac{\partial I(s,\Omega)}{\partial s} = -E(s,\Omega)I(s,\Omega) + \frac{1}{4\pi}\int_{4\pi} I(s,\Omega')G(s,\Omega',\Omega)d\Omega' + F(s,\Omega) \tag{1.14}$$

that is the general form of the equation of radiative transfer.

In planetary applications the medium is usually horizontally stratified. Let the positive z axis point in vertical direction, and let ds make an angle ϑ with dz, so that $dz = ds\cos\vartheta$ as shown in figure 1.1. Making this substitution and dividing by $E(z)$, defined in analogue mode of equation (1.11), gives

$$\frac{\cos\vartheta}{E(z)}\frac{\partial I(z,\Omega)}{\partial z} = -I(z,\Omega) + \frac{S(z)}{E(z)}\frac{1}{4\pi}\int_{4\pi} I(z,\Omega')\frac{G(z,\Omega',\Omega}{S(z)}d\Omega' + \frac{F(z,\Omega)}{E(z)} \tag{1.15}$$

In order to emphasizing in the equation (1.15) the particles role in the process, we define the *optical depth*, τ, defined as

$$\tau = \int_s^\infty E(s')ds'/\cos\vartheta = \int_z^\infty E(z')dz', \tag{1.16}$$

so that

$$d\tau = -E(s)ds/\cos\vartheta = -E(z)dz, \tag{1.17}$$

where τ is a dimensionless vertical distance expressed in units of extinction length $1/E$. The altitude z can be expressed equivalently in terms of τ. Radiance emitted vertically upward at altitude z within the scattering medium is reduced of a factor $e^{-\tau}$ by extinction as it propagates to the top of the medium.

We define also $w(z)$ be the *volume single-scattering albedo*,

$$w(z) = S(z)/E(z), \tag{1.18}$$

and $p(z, \Omega', \Omega)$ be the *volume phase function*,

$$p(z, \Omega', \Omega) = G(z, \Omega', \Omega)/S(z) \tag{1.19}$$

Finally the *source function* could be defined by

$$\mathcal{F}(z, \Omega) = F(z, \Omega)/E(z) = Je^{-\tau/\cos i} w(\tau) p(\tau, \Omega_0, \Omega) \mathcal{F}_T(z, \Omega) \tag{1.20}$$

where i is the angle between the incident irradiance and the vertical, and

$$\mathcal{F}_T = F_T/E. \tag{1.21}$$

that represent the scattering fraction of the volume emission coefficient.
Then the equation of the radiative transfer may be written as

$$\begin{aligned} -\cos\vartheta \frac{\partial I(\tau, \Omega)}{\partial \tau} = & - I(\tau, \Omega) + \tfrac{w(\tau)}{4\pi} \textstyle\int_{4\pi} I(\tau, \Omega') p(\tau, \Omega, \Omega') d\Omega' \\ & + J \tfrac{w(\tau)}{4\pi} p(\tau, \Omega_0, \Omega) e^{-\tau/\cos i} + \mathcal{F}_T(\tau, \Omega). \end{aligned} \tag{1.22}$$

1.2.1 Radiative transfer in a particulate medium

If the medium is uniform, the volume absorption coefficient is coincident with the ordinary absorption coefficient: $K = \alpha = 4\pi k/\lambda$, where k is the imaginary part of refractive index. The extinction or scattering coefficients then have physical

meanings similar to α. The intensity of a collimated beam of radiation penetrating through the material will be reduced by a factor of e^{-1} in a distance $1/K$, if only absorption is present, in a distance $1/S$, if only scattering occurs, or in a distance $1/E = 1/(S + K)$ if there is a combination of absorption and scattering. These definitions are inadequate if the medium is nonuniform and, in particular, if it consists of particles that are large compared with the wavelength. We can work with the following approach: suppose that the medium consists of identical particles separated by random distances that are, on the average, large compared with both the particle size and the wavelength; suppose that in a volume $dsdA$ are present N particles, per unit volume, with a *geometric cross-sectional area* σ, so that the total number of particles is $NdsdA$. If J is the intensity of the incident light, the extinguished power fraction ΔP_E is given by

$$\Delta P_E = dJd\Omega dsdA = JN\sigma Q_E dsdAd\Omega \tag{1.23}$$

where Q_E is the *extinction efficiency*, defined as the ration between *extinction cross section*[4] and the cross-sectional area, $Q_E = \sigma_E/\sigma$. The comparison between equations (1.23) and (1.4) suggest that the volume extinction coefficient for a particulate medium may be defined as

$$E = N\sigma Q_E. \tag{1.24}$$

More generally, if the slab contains a mixture of different particles with N_j particles of type j per unit volume, geometric cross section σ_j, and extinction efficiency Q_{Ej},

[4]The extinction cross section is the ratio between the extinguished power (P_E) and the incidence irradiance (J), $\sigma_E = P_E/J$

the volume extinction coefficient is defined as

$$E = \sum_j N_j \sigma_j Q_{Ej} = N\langle \sigma Q_E \rangle. \tag{1.25}$$

Where $N = \sum_j N_j$ is the total number of particle per unit volume, and $\langle \sigma Q_E \rangle = (\sum_j N_j \sigma_j Q_{Ej})/N$ is the average extinction cross section.

Similarly, we can define

$$S = \sum_j N_j \sigma_j Q_{Sj} = N\langle \sigma Q_S \rangle \tag{1.26}$$

$$K = \sum_j N_j \sigma_j Q_{Aj} = N\langle \sigma Q_A \rangle \tag{1.27}$$

$$G(g) = \sum_j N_j \sigma_j Q_{Sj} p_j(g) = N\langle \sigma Q_S p(g) \rangle \tag{1.28}$$

where Q_{Sj} and Q_{Aj} are, respectively, the *scattering* and *absorption efficiencies* of the j^{th} type of particle.

We have ample reason to believe that the particulate materials, in nature, are well packed. Therefore we can describe our system as formed by particles, large respect the wavelength and with arbitrary separation. We then introduce the *filling factor* (i.e. the total fraction of volume occupied by the particles) that can be described by the equation

$$\phi = \frac{4\pi a^3}{3Z^3} \tag{1.29}$$

with $Z = N^{-1/3}$, representing the mean distance between particles. If we introduce the effective particle density, defined by

$$N_E = -N\frac{\ln(1-\phi)}{\phi}. \tag{1.30}$$

When $\phi \ll 1$, $\ln(1-\phi) \simeq \phi$ and E assumes its usual form. However, as $\phi \to 1$, the surface becomes opaque and the sample could be described as bulk. With this assumption we can write

$$E = N_E \langle \sigma Q_E \rangle. \tag{1.31}$$

1.3 Hapke theory of reflectance

The term *reflectance* and *reflectivity* both refer to the fraction of incident light scattered or reflected by a material. Although they are sometimes used interchangeably, reflectance has the connotation of the diffuse scattering of light in many directions by a geometrically complex medium, whereas reflectivity refers to the specular reflection of radiation by a smooth surface. We can define several types of reflectance, depending on geometry. Usually the world reflectance is preceded by two adjectives, the first describes the degree of collimation of the source, the second that of the detector. We will focalize our attention on bidirectional, the most ideal, and directional hemispherical reflectance, our instrumental suit. For the derivation of the bidirectional reflectance we will use the geometry shown in figure 1.2. Collimated light (irradiance) J from a source of radiation is incident on the upper surface of a scattering medium. The normal to the surface N is parallel to the z axis, and the incident light makes an angle i with N. The light interacts with the medium, and some of the rays emerge from an element ΔA of the surface traveling toward a detector in a direction that makes an angle e with N. The plane containing the incidence ray and N is the *plane of incidence*, while that containing the emerging rays and N is the *plane of emergence*. The azimuthal angle between those two planes is ψ and the angle between the direction to the source and that of

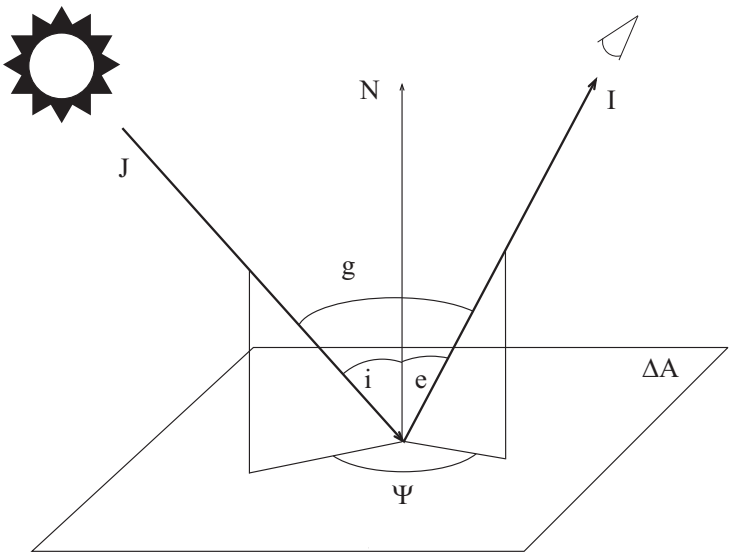

Figure 1.2: Geometry for derivation of bidirectional reflectance formula.

the detector, as seen from the surface, is the phase angle g. The plane containing the incidence and the emergence rays is the *scattering plane*. If the planes of incidence and emergence coincide ($\psi = 0$ or $180°$), their common plane is called *principal plane*. Usually, instead of i and e, are used the derived variables

$$\mu = \cos e \tag{1.32}$$

$$\mu_0 = \cos i \tag{1.33}$$

Following the definition given at the begin of this section we can write reflectance as

$$r(i, e, g) = I_D/J \tag{1.34}$$

where I_D is the irradiance to the detector, defined as the power per unit area per unit solid angle. The irradiance, calculated by the integration of the power at detector,

P_D, in our case is

$$I_D = \frac{1}{\Delta w \Delta a} \int_{z=-\infty}^{\infty} dP_D = -\mu e^{-\tau/\mu} \frac{\partial}{\partial \tau} \left[I(\tau, \Omega) e^{-\tau/\mu} \right] = I(0, \mu) \tag{1.35}$$

so that (1.34) becames

$$r(i, e, g) = I(0, \mu)/J. \tag{1.36}$$

The radiance, as solution of equation (1.22) (Hapke, 1993), could be written as

$$\begin{aligned} I(\tau, \Omega) &= I(\tau, \cos\vartheta) = \frac{Jw}{4\pi} \frac{1}{4\gamma^2\mu_0^2 - 1} \left[-\frac{(1-\gamma)2\mu_0(1+2\mu_0)}{1+2\gamma\cos\vartheta} e^{-2\gamma\tau} + \right. \\ &+ \left. \frac{\mu_0}{\mu_0 + \cos\vartheta} (4\mu_0^2 - 1) e^{-\tau/\mu_0} \right]. \end{aligned} \tag{1.37}$$

Substituting (1.37) in (1.36), the expression for $r(i, e, g)$ becomes

$$r(i, e, g) = \frac{w}{4\pi} \frac{\mu_0}{\mu_0 + \mu} \frac{1 + 2\mu_0}{1 + 2\gamma\mu_0} \frac{1 + 2\mu}{1 + 2\gamma\mu}. \tag{1.38}$$

If we introduce the function

$$H(x) = \frac{1 + 2x}{1 + 2\gamma x} \tag{1.39}$$

called *Chandrasekhar function* and describing the isotropic scattering (Chandrasekhar, 1960). The equation (1.38) becomes

$$r(i, e, g) = \frac{w}{4\pi} \frac{\mu}{\mu + \mu_0} H(\mu) H(\mu_0). \tag{1.40}$$

If we, also, consider non isotropic scattering, we must introduce (1.40) the *phase function*, $p(g)$, defined in (1.19), obtaining

$$r(i,e,g) = \frac{w}{4\pi}\frac{\mu_0}{\mu+\mu_0}\left[p(g) + H(\mu)H(\mu_0) - 1\right]. \tag{1.41}$$

In the geometry of directional-hemispherical reflectance we collect all the back scattered radiation, that means

$$r_h(i) = \frac{1}{\mu_0}\int_{2\pi} r(i,e,g)\mu d\Omega_e, \tag{1.42}$$

where $d\Omega_e = \sin e \; ded\psi$.

Substituting equation (1.41) r in (1.42) we obtain

$$r_h(i) = \frac{w}{4\pi}\int_{\psi=0}^{2\pi}\int_{e=0}^{\pi/2}\frac{\mu}{\mu_0+\mu}\left[p(g) + H(\mu_0)H(\mu) - 1\right]\sin e \; ded\psi. \tag{1.43}$$

Integrating equation (1.43), as described by Hapke (1981), we obtain

$$r_h(i) = \frac{1-\gamma}{1+2\gamma\mu_0} \tag{1.44}$$

where γ, called *albedo factor*, is given by

$$\gamma = \sqrt{1-w}. \tag{1.45}$$

This expression was first obtained by Reichman (1973).

Chapter 2

Dimensional Contamination

In this chapter we discuss the procedure used for the production of the examined samples and the problems linked to the determination of the actual grainsize. We also describe a procedure aimed to obtaining a good gaussian law for the grain size distribution.

2.1 Sample characterization parameters

The dust analysis is a problem common to many fields of research in astrophysics, from the molecular clouds study (Chapman & Wardle, 2006; Nozawa *et al.* , 2006) to the planetary exploration (Maturilli *et al.* , 2006). For the interpretation of the observed data, it is usual to compare laboratory and observed spectra, applying an adequate radiative transfer model. We can define some parameters characterizing our sample and describing sample from different points of view:

a) *Purity*;

b) *Mean diameter*;

c) *Coefficient of Uniformity*;

d) *Coefficient of Curvature*.

Purity describes the distance between the chemical composition of the sample and the stechiometric formula. The evaluation of this parameter is performed by EDX analysis (Energy Dispersive X-ray analysis). The *mean diameter* describes the dimension of the particles forming the sample. Procedures for the production of a sample do not produce particles of a single diameter but a distribution of different sizes. For this reason it is not simple defining a mean diameter. We can introduce an equation that could describe many different mean diameters:

$$D[m,n] = \left[\frac{\sum d_i^{m-3}\mathcal{V}_i}{\sum d_i^{n-3}\mathcal{V}_i}\right]^{\frac{1}{(m-n)}} \tag{2.1}$$

where $\mathcal{V}_i$ is the volume of particles with size d_i, m and n are integer values that describe the average being used (Zhou *et al.* , 2006). The most used couples of (m,n) are $(4,3)$ and $(3,2)$ (Allen, 1999; Gabas *et al.* , 1994). From the couple $(4,3)$ we obtain the De Brouckere mean diameter, or volume moment mean, $D[4,3]$, representing the diameter of the mean equivalent sphere, in volume, of the size distribution of a grain sample, and is given by the formula:

$$D[4,3] = \frac{\sum d_i^4}{\sum d_i^3} \tag{2.2}$$

(Alderliesten, 1991).

From the couple $(3,2)$ we obtain the Sauter diameter, the diameter of a equivalent

sphere, in surface, given by the formula:

$$D[3,2] = \frac{\sum d^3}{\sum d^2}. \tag{2.3}$$

The errors connected to the De Brouckere and Sauter diameter are given by the following expressions:

$$\Delta D[3,2] = \sum_j \frac{3d_j^2 \sum_i d_i^2 - 2d_j \sum_i d_i^3}{\left[\sum_i d_i^2\right]^2} \Delta d_j \tag{2.4}$$

$$\Delta D[4,3] = \sum_j \frac{4d_j^3 \sum_i d_i^3 - 3d_j^2 \sum_i d_i^4}{\left[\sum_i d_i^3\right]^2} \Delta d_j \tag{2.5}$$

with Δd_j linked to the sensibility of the instrument. The laser diffraction system, used for the derivation of the diameters, could be divided into two sub system. The first is a particle counter based on the on-off status of the laser ray. Each particle, following the dispersant flow, interrupts the laser beam giving the information. The second sub-system gives information on the size in function of the laser deviation due to diffraction from the particle. Smaller grains produce a large diffraction angle. The detector is made of a set of 50 circular concentric sensor of different size, proportional to the radius. So for a given diameter range a single sensor is involved. The uncertainty associated to the measure is strongly influenced by the instrumental procedure. For this reason each measurement is the mean of 5000 different measurements.

It is possible to define custom parameters by using of a code writing in a proprietary develop environment. Such parameters are available in real time during the measurement. In the following, we report the scripts for the $D[3,2]$ and $D[4,3]$ standard deviations.

Listing 2.1: Custom function for the standard deviation of the Sauter diameter.

```
1 Option Explicit
2 Private Function Calc() As Variant
3     Dim volsd As Variant
4         volsd= Stats.StandardDeviation(rtSurface)
5         'Round returns the calculated value to 3 decimal places
6         Calc =Round (volsd ,3)
7 End Function
```

Listing 2.2: Custom function for the standard deviation of the De Brouckere diameter.

```
1 Option Explicit
2 Private Function Calc() As Variant
3     Dim volsd As Variant
4         volsd= Stats.StandardDeviation(rtVolume)
5         'Round returns the calculated value to 3 decimal places
6         Calc =Round (volsd ,3)
7 End Function
```

The *Coefficients of Uniformity* (Cu) and *Curvature* (Cc) are parameters that describe the shape of a given particle size distribution curve. Cu is equal to D_{60}/D_{10}[1]. Cc is equal to $(D_{30}^2)/(D_{10} \cdot D_{60})$. If the materials tested are highly uniform (i.e., $Cu < 2$) it means that the particle population has very little variation in size. An high degree of uniformity is desirable for a good packing of the grains, since little or no segregation of particles, by size, can occur during sample preparation and typically pressure head loss is less through more uniform well packing. For the derivation of those parameters we defined the scripts (listing 2.3) and (listing 2.4).

[1]The symbol D_{xx} is used for the diameter below which there are the xx % of the sample particles, and is called percentile xx.

Listing 2.3: Custom function for the uniformity definition.

```
1  Option Explicit
2  Private Function Calc() As Variant
3      Dim A As Variant
4      Dim B As Variant
5      A = Stats.Percentile(60)
6      B = Stats.Percentile(10)
7      Calc = Round(A/B,3)
8  End Function
```

Listing 2.4: Custom function for the curvature definition.

```
1  Option Explicit
2  Private Function Calc() As Variant
3      Dim A As Variant
4      Dim B As Variant
5      Dim C As Variant
6      A = Stats.Percentile(10)
7      B = Stats.Percentile(30)
8      C = Stats.Percentile(60)
9      Calc = Round((B^2/(A*C)),3)
10 End Function
```

2.2 Sample preparation

The procedure to produce the grains is in 3 steps: 1) *row fragmentation*, 2) *grinding*, 3) *sieving*.

In the *row fragmentation* we break the bulk rock with a hammer obtaining pieces of a size around few millimeters. The material resulted is put in a grinder (Retsch Mortar Grinder RM 100, see section 2.3.1) capable to produce, by various cycles, powder of a size around 1 μm. The so obtained sample is introduced in an automatic dry sieve (Retsch Sieve Shaker AS 200 basic, see section 2.3.1) that permits to select

samples with different grain size ranges. In particular our instrument is equipped to produce the grain sizes listed in table 2.1.

Table 2.1: Dimensional classes obtained by sieving the produced dust.

Dimensional class	
A	450 ÷ 300 μm
B	300 ÷ 200 μm
C	200 ÷ 106 μm
D	106 ÷ 50 μm
E	50 ÷ 20 μm

The choice of the listed dimensional classes is made according to the dimensional classification of Udden-Wentworth (Wenthworth, 1922) with some adjustments due to the availability of the right sieve. In table 2.2 we report such classification for our ranges. For the complete Udden-Wentworth classification see appendix A

Table 2.2: Udden-Wentworth classification extract for the grain from 500 to 16 μm.

Dimension	Name
500 ÷ 250 μm	medium sand
250 ÷ 125 μm	fine sand
125 ÷ 62 μm	very fine sand
62 ÷ 31 μm	coarse silt
31 ÷ 16 μm	medium silt

We have also introduced a separation of the medium sand grain size range in two

subranges ($400 \div 300$ μm and $300 \div 200$ μm) for planetalogical purposes. In fact the mean grain size of the surface dust of Mars is between 300 and 100 μm (Jakosky *et al.* , 2000) and therefore we prefer to analyze the medium sand interval in more detail.

With this procedure we obtain also two dimensional classes that are the residual of the sieving procedure. Sauch classes include the grains bigger than 425 μm and smaller than 20 μm corresponding, respectively, to the content of the first sieve and of the bottom container. The first residual is then used for another process of particles production while the finest one is used to obtain, after further separation processing, particles with dimensions of the order of one micron, used for the study of the areosol.

After the production of particles, we perform a control of the grain population in the different dimensional ranges with a granulometer based on laser diffraction (Malvern Mastersizer 2000) whose description is reported section 2.3.2. Performing this measurement is not unusual to obtain a bimodal distribution due to the presence of small grains, as it is possible to see in figure 2.1, where the small grain family is quite evident.

This family is formed in the grinding process and not easily separated. In fact, in the sieving process, the bigger grains capture the smaller grains due to the electrostatic charge acquired during the grinding procedure. On the other hand, when the sample is introduced in the granulometer, the charges are neutralized by the polarity of the dispersant (in our case water) and the smaller grains become free originating the secondary population.

The presence of the secondary population, produces some spectroscopical effects that can introduce some bias in the transfer model. For this reason we analyze the

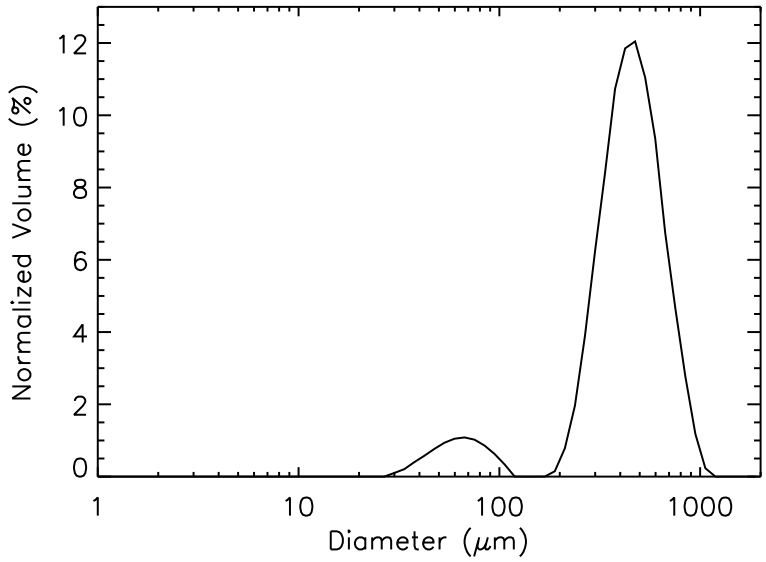

Figure 2.1: Grain size distribution for a sample in the nominal size range 300 ÷ 200 μm.

modifications of the spectra due to the decreasing uniformity of the sample.

2.3 Instumentation

2.3.1 Fragmentation and sieving

To obtain the fragmentation of the rock, after a raw crumble obtained with a hammer, we use a Retsch Mortar Grinder RM 100, whose scheme is reported in figure 2.2.

The RM 100 comminutes, mixes and triturates by pressure and friction. The function of the scraper is to feed the material into the area between the mortar and pestle. This forced feed ensures that the whole sample is continuously subjected to the grinding and trituration process and is also intensively mixed. The pestle is not located in the centre of the mortar but is offset; in contact with the rotating mortar and the sample causes it to rotate automatically. The necessary grinding pressure

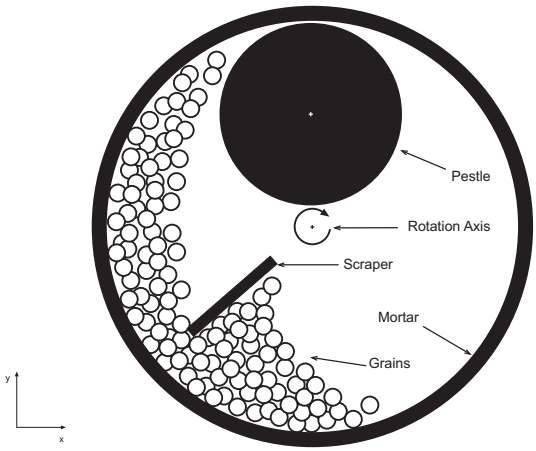

Figure 2.2: Grinder scheme.

is achieved by the weight of the pestle itself combined with the adjustable spring pressure acting on its axis.

The powder obtained with the grinder is processed by the sieve Retsch Sieve Shaker AS 200 basic. The sieve shakers work with an electromagnetic drive that produces a 3D throwing motion moving the product to be sieved equally over the whole sieving surface. The advantages are high stress capacity, extremely smooth operation and short sieving times with high separation efficiency. The classes obtained with this process are produced by the different grid of each stadium.

2.3.2 Laser diffractometer

The laser diffractometer is based on the scattering theory of Lorenz-Mie (Bohren & Huffman, 1983; van de Hulst, 1957; Kerker, 1969), where the diffraction angle of the incident light depends on wavelength as well as the diameter and the material of the particle. If we use a laser source (high coherence, high directionality, very small divergence and a single and well definite wavelength) and work with a mineral, i.e. a material with a well known complex refractive index (Palik, 1985, 1991), we can

relate the diffraction angle only to the size of the particles.

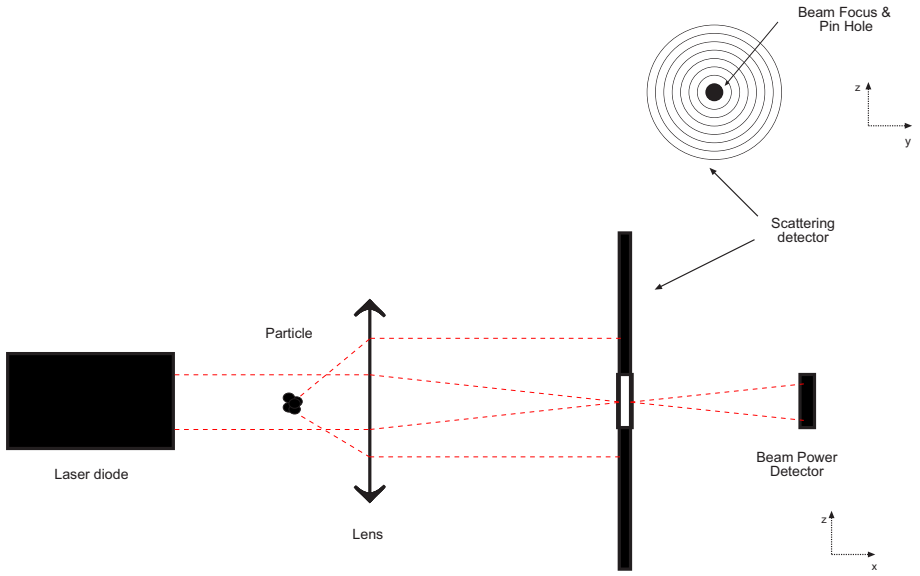

Figure 2.3: View of the optical scheme of the diffractometer along the axis parallel to the laser beam

In figure 2.3 is reported the scheme of the laser diffractometer along the axis parallel to the laser beam. The instrument source consist of two laser, a 10 mW helium-neon at 632.8 nm and a solid state source at 466 nm. The laser beam passes through a cell in which the powder is dispersed and in which the scattering takes place. This cell is connected to the sampler that activates the flux of the particles and the dispersant through in the cell and permits, in automatic mode, several cycles of measurement. We have two different samplers, dry and wet, according to the dispersant used that could be air, for the dry, or a fluid, like water or alcohol, for the wet. In the last case the refractive index of the dispersant is introduced in the Scattering equation. In our case we use the wet sampler, Malvern Hydro 2000, with different dispersant according to the nature of the mineral grains. A converging lens, that focalizes the beam on the detector, is located after the cell. The scattering detector is an array of fifty circular and concentric sensors, as shown in the view normal to the laser beam

in the upper side of figure 2.3. This particular shaping permits the measurement of the scattering along all solid angles. Other detectors are located in particular positions and permit to detect the wide angle scattering and the backscattering (Ran, 1998).

2.3.3 Spectrometers

For the spectral analysis we use two different spectrometers for two different wavelength ranges. The first is a grating spectrometer (Perkin Helmer Lambda 900) covering the range from 0.2 to 2.5 μm. On the spectrometer can be mounted an optical bench PELA 1000 with a Labsphere integrating sphere, 13 cm in diameter, in Spectralon (see paragraph B.1) with an incidence angle of 8°. The measurements are performed with the setup reported in table 2.3.

Table 2.3: Setup for the Perkin-Elmer Lambda 900 spectrometer.

Parameter	**Value**
Range	0.2 ÷ 2.5 μm
Integration time (Visible)	0.04 s
Slit mode	Fix
Slit	2 nm
Integration time (Infrared)	0.12 s
Slit mode	Auto
Gain	4

The second instrument is a *Fast Fourier Transforms* (FFT) spectrometer (Perkin Elmer Spectrum 2000) equipped with a Labsphere integrating sphere in Infragold

(see paragraph B.2) with an incidence angle of 13°. In this configuration the instrument covers the range between 1.7 and 25.0 μm. The setup for this instrument is reported in table 2.4.

Table 2.4: Setup for the Perkin-Elmer Spectrum 2000 spectrometer.

Parameter	**Value**
Range	$1.7 \div 25.0$ μm
Resolution	4 cm^{-1}
Beam splitter	KBr
J-Stop	6.48 cm^{-1}
Apodizathion	Strong
Gain	8
OPD velocity	0.2 cm/s

As shown in tables 2.3 and 2.4 the two ranges overlaps in the region between 1.7 and 2.5 μm. This choice is really useful for the comparison of the spectra produced by the two instruments, since allows to compare directly the continuum of the two spectra. Usually the two continuum levels are very close to each other, after the normalization to the reflectivity of the two different materials used as reference. The difference is always below 3%, that is also the error associated to the repeatability of the measurements.

2.4 Samples

For this campaign we choose a material of planetary interest, quartz (SiO_2), which is not actually present on the surface as outcrops, but it is used for the simulation of rocks with an high-Si glass contents (Christensen *et al.* , 2005). In quartz crystals there are only six $Si - O - Si$ bonds per cell and this brings as a consequence that the resulting spectrum is not very complex. In table 2.5 reports the lattice vibration in middle infrared range are reported (Farmer, 1974).

Table 2.5: Lattice vibration in quartz.

Species	**IR spectrum** (cm^{-1})	**Species**	**IR spectrum** (cm^{-1})
A_2	373	E	462
A_2	512	E	697
A_2	780	E	798
A_2	1150	E	1084
E	264	E	1172
E	398		

In figure 2.4 the results of the EDX analysis of our sample are shown. The panels are sorted according to the nominal grain sizes as reported in table 2.1. We can see that the differences are really small. In fact there is only a difference in counts in the the two bands at 1.75 KeV for Sik[2] and 0.52 KeV for Ok (see table 2.6), but

[2]In the EDX analysis a peak corresponding to the amount of energy possessed by X-rays emitted by an electron in the L-shell of the atom going down to the K-shell is identified as a Kα peak. The peak corresponding to X-rays emitted by M-shell electrons going to the K-shell is identified as a

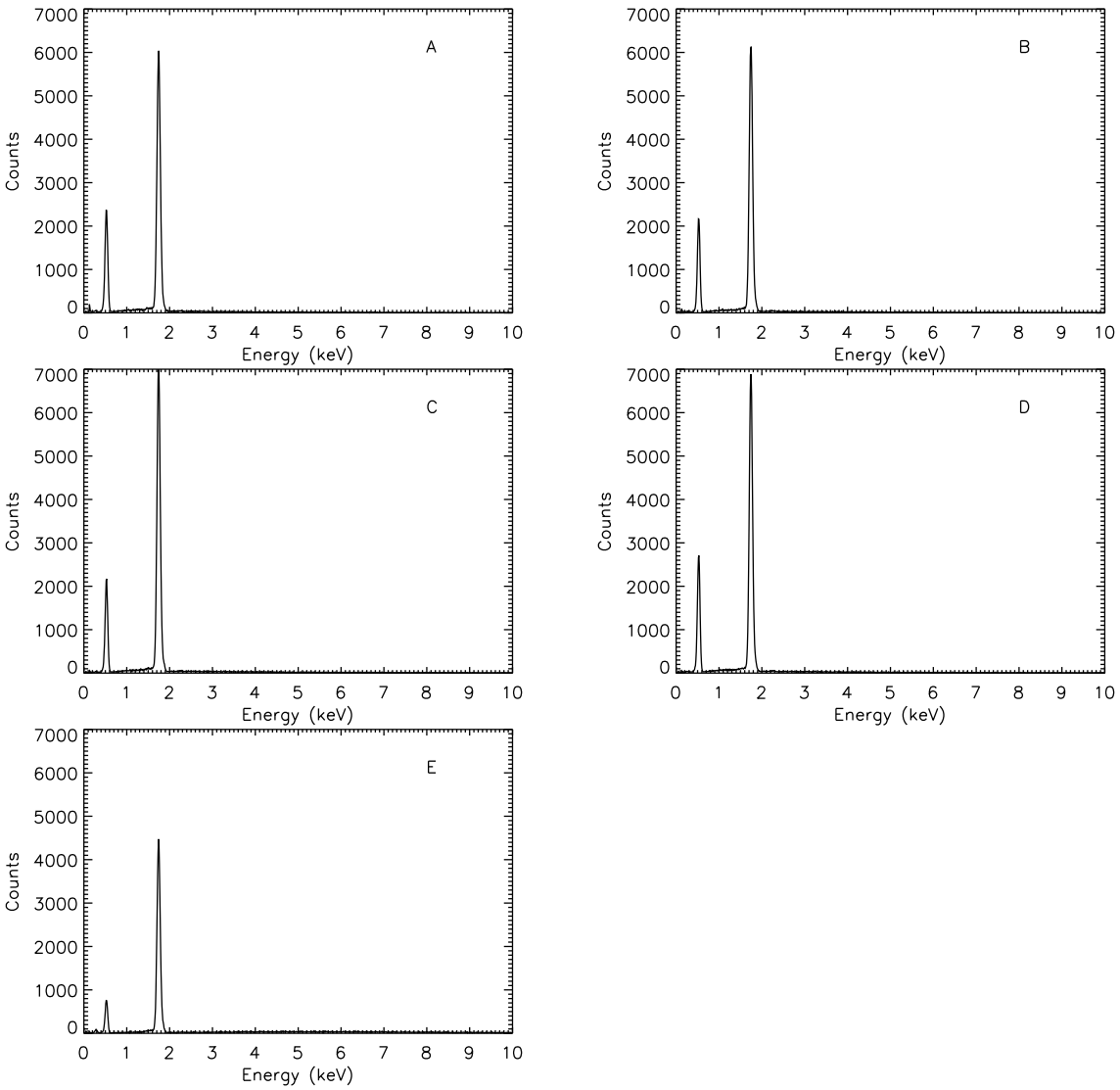

Figure 2.4: EDX analysis of the different grain size family sorted according to table 2.1. We can see only the presence of the Sik and Ok bands as demonstration of an high purity of the samples.

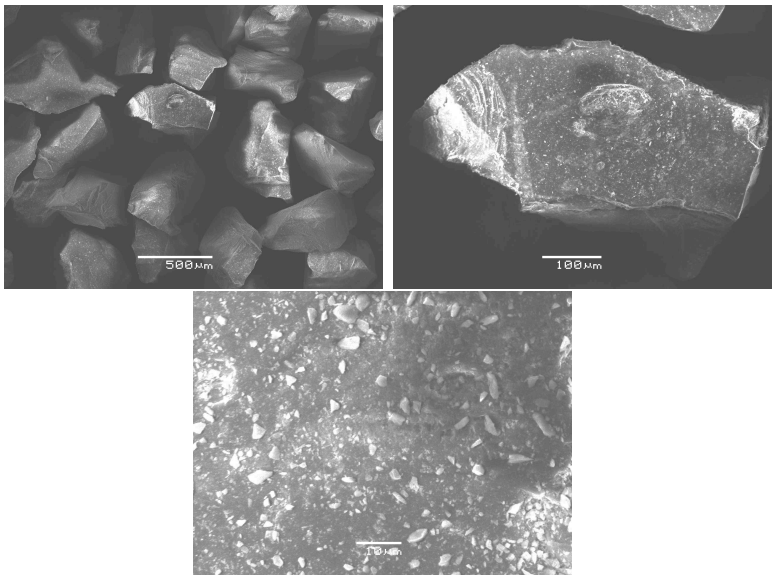

Figure 2.5: Some SEM image of the sample at different magnifications are shown. The presence of small grain attached to the bigger one is evident.

are not present bands due to impurity. The counts are higher in the samples with a sieve diameter between 200 and 106 μm (figure 2.4-C) and between 106 and 50 μm (figure 2.4-D), lower in the sieve diameter between 50 and 20 μm (figure 2.4-E). For these reasons, we can define our sample as an high purity quartz.

Table 2.6: Sik and Ok counts values and respective energies.

Sik counts	**Energy (KeV)**	**Ok counts**	**Energy (KeV)**
6037	1.74	2374	0.52
6133	1.75	2164	0.52
7123	1.74	2172	0.53
6885	1.74	2708	0.53
4473	1.74	754	0.52

Kβ peak. Usually the α is omitted and is explicit form only the β case. In the name of the peak is also not used the capital letter K to not mistake with chemical symbol of potassium.

2.5 Data analysis

By performing the grain size analysis with the laser diffractometer, we obtain the curves reported in figure 2.6 and the data summarized in table 2.7.

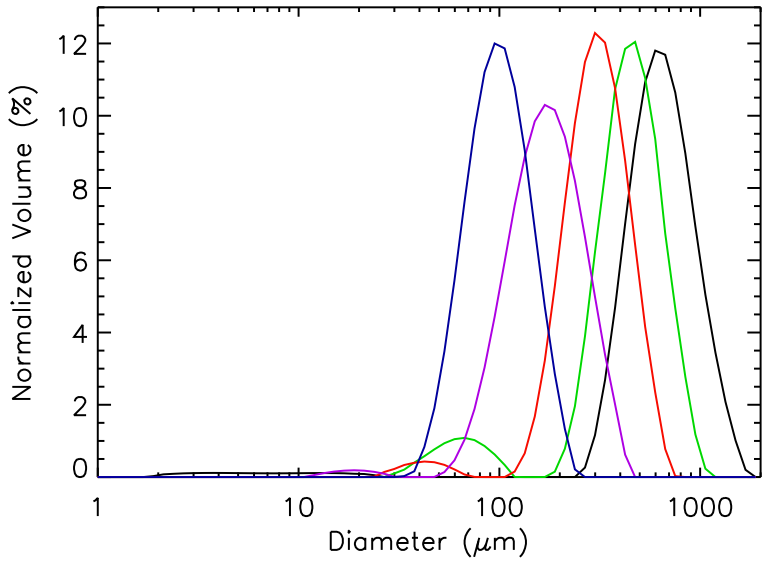

Figure 2.6: Comparison of the equivalent volume distribution of the different grain size range. The black line is the range 450 ÷ 300 μm, the green line the range 300 ÷ 200 μm, the red line is the range 200 ÷ 106 μm, the violet line is the range 106 ÷ 50 μm and the blue line for the range 50 ÷ 20 μm.

Table 2.7: Morphological parameter for the different size classes defined in section 2.1.

Sample	$D[3,2](\mu m)$	$D[4,3](\mu m)$	Cu	Cc
425 ÷ 300 μm	287.887	448.678	1.998	1.098
300 ÷ 200 μm	249.481	316.817	1.799	1.002
200 ÷ 106 μm	143.072	181.557	1.986	0.993
106 ÷ 50 μm	91.773	104.114	1.766	0.980
50 ÷ 20 μm	14.925	35.806	6.481	1.611

With the aim to understand the dimensional purity of the samples we report in figure 2.7 the comparison, for each dimensional class, between different size distribution. In particular we report the equivalent volume distribution, the equivalent surface and length. We also show the numerical distribution with the aim to understand the number of particles for each diameter. We can see that only for the class between $106 \div 50$ μm (panel 2.7-D) we have a dimensional purity denoted by the closing of the peak of the distributions.

The spectral analysis of the samples is performed in directional hemispherical reflectance (Hapke, 1981, 1993) in the range between 0.2 and 25.0 μm with the spectrometers described in section 2.3.3. In figure 2.8 are reported the spectra of the various dimensional classes, in the range between 0.2 and 2.5 μm. It is apparent from figure 2.8, that the levels of the continuum in the flat region (from 0.7 μm to the end of the range) are really close, with a variation between 73 % and 77 % of reflectance. In the short wavelength part of the spectra the difference due to the grain size is more evident, in particular for the band at 0.254 μm. If we compare the depth of this band, versus the dimension of the grains, to the level of the continuum we find a linear trend, as shown in figure 2.9, with the exception of the finest grains.

The spectra collected, for the same samples, in the range between 1.7 and 25.0 μm are reported in figure 2.10. We note that all the spectra have almost the same continuum level at the short wavelength end of the range, according to the trend evidenced in figure 2.8, but in the band around 3.0 μm they already present a significative divergence. In the region between 5 μm and 7.4 μm, the Christiansen frequency of quartz (Salisbury *et al.* , 1987), the spectra are really close, except for the finest size class. And the same trend is shown in the restrahlen bands at 8.5, 12.4 and 21.0 μm (Farmer, 1974). These trends are as expected: in fact the restrahlen

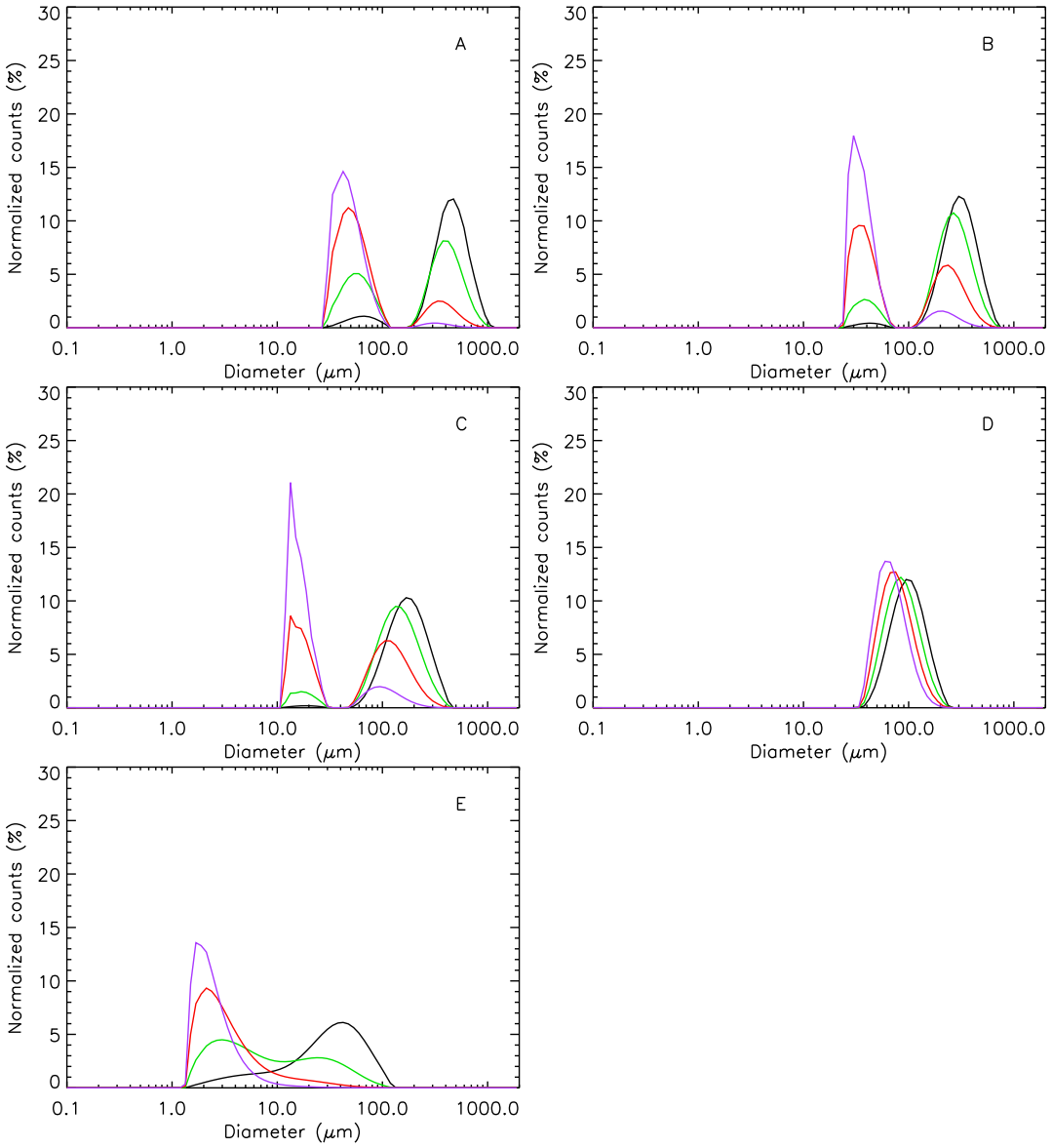

Figure 2.7: Plot of the normalized counts for the samples grain size ranges sorted according to table 2.1. The black line is the equivalent volume distribution, the green line is the equivalent surface distribution, the red line is the length equivalent distribution and the violet line is the number distribution.

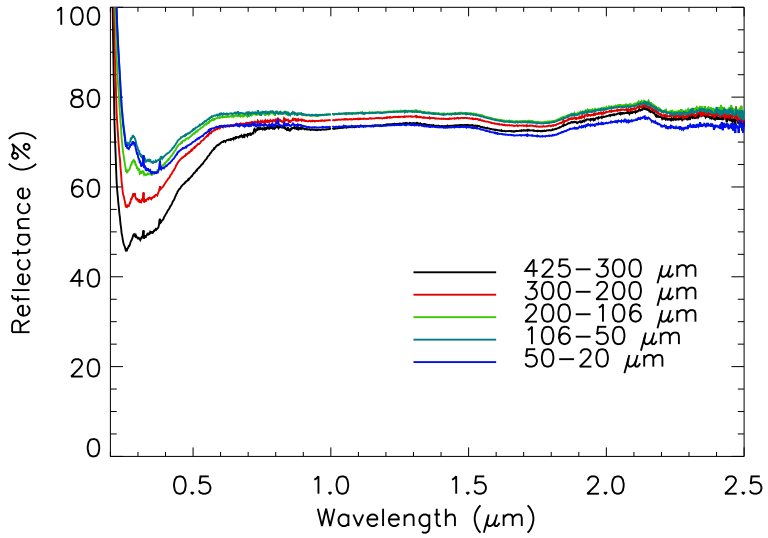

Figure 2.8: Spectra of the different dimensional classes of the quartz sample in the spectral range $0.2 \div 2.5$ μm.

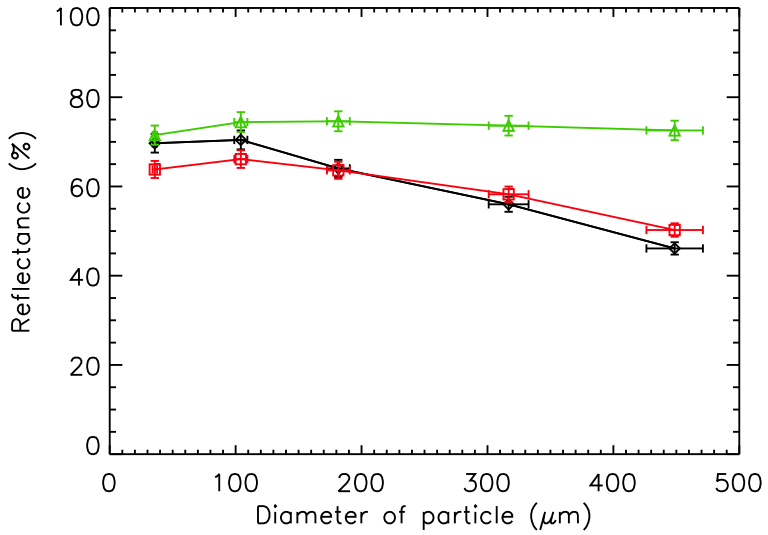

Figure 2.9: Level of the reflectance of the spectra at 0.254 μm (black line), at 0.350 μm (red line) and at 1.70 μm (green line) versus the grain size. The wavelength at 1.70 μm give us information about the continum level.

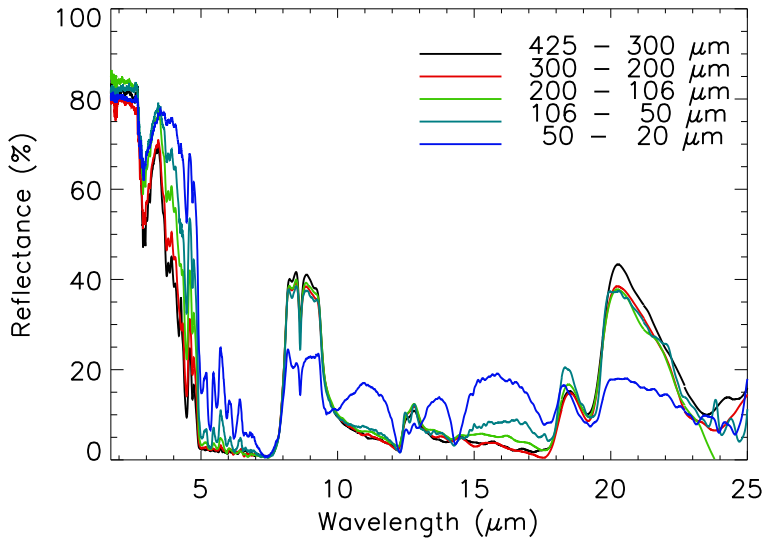

Figure 2.10: Infrared spectra of the different dimensional class (see table 2.1) of the quartz sample in the spectral range 1.7 ÷ 25.0 μm.

intensity is directly related to the grain dimension (Hapke, 1993) (see figure 2.11). However, the difference among the dimensional classes, excluding the finest grains, is considerably less than expected taking also into account the wide range covered (from 450 to 50 μm).

At this point we applied a procedure of dimensional purification consisting in washing repeatedly the samples. The particulate material is suspended in a cuvette filled with ethylic alcohol at 99.9% and put in to a centrifuge. The alcohol is not a polar dispersant, but the action of the centrifuge facilitates the separation of different grainsize families. Moreover, the high level of volatility of ethylic alcohol is useful for increasing the speed of the sample preparation process.

After the washing procedure the grainsize families have been checked again with the laser diffraction and the results are shown in figure 2.12 while the relative data are reported in table 2.8.

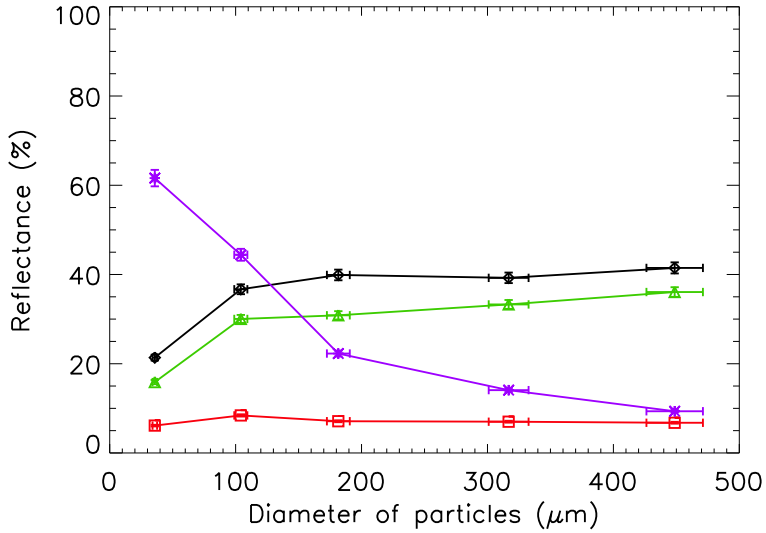

Figure 2.11: Level of the reflectance of the spectra at the restrahlen bands versus the grain size. In particular at 8.5 μm (black line), at 12.4 μm (red line) and at 21.0 μm (green line). For comparison the trend at 4.47 μm (violet line), corresponding to an absorption band, is also added.

Table 2.8: Morphological parameter for the different size classes for washed samples.

Sample	$D[3,2](\mu m)$	$D[4,3](\mu m)$	Cu	Cc
425 ÷ 300 μm	436.384	470.959	1.538	0.985
300 ÷ 200 μm	298.297	327.335	1.618	0.983
200 ÷ 106 μm	174.941	197.273	1.738	0.980
106 ÷ 50 μm	91.976	104.362	1.766	0.980
50 ÷ 20 μm	22.919	41.959	3.209	1.166

If we compare the figures 2.7 and 2.12 we can easily see the effects of the washing procedure. To increase the data readability we report in table 2.9 a comparison of the uniformity and curvature between the unwashed and the washed samples.

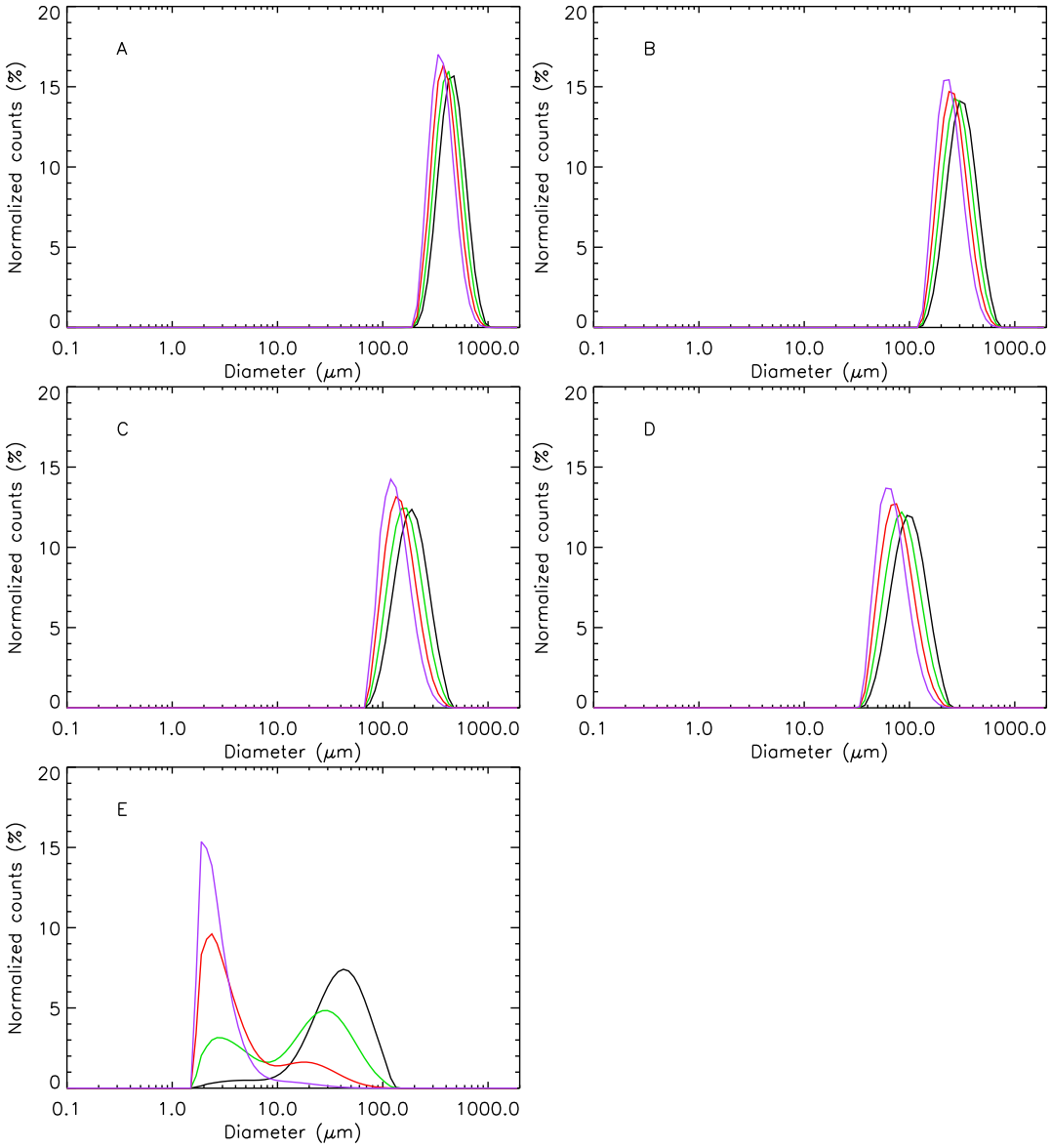

Figure 2.12: Grain families after the washing procedure.

Table 2.9: Comparison of the uniformity and curvature between the unwashed and the washed samples.

C_u		C_C	
not washed	**washed**	**not washed**	**washed**
1.998	1.538	1.098	0.985
1.799	1.618	1.002	0.983
1.986	1.738	0.993	0.980
1.766	1.766	0.980	0.980
6.481	3.209	1.611	1.166

We also report in table 2.10 the same comparison for the Sauter and De Brouckere mean diameters.

Table 2.10: Comparison of the $D[3,2]$ and $D[4,3]$ between the unwashed and the washed samples.

$D[3,2]$		$D[4,3]$	
not washed	**washed**	**not washed**	**washed**
287.887	436.384	448.678	470.959
249.481	298.297	316.817	327.335
143.072	174.941	181.557	197.273
91.773	91.976	104.114	104.362
14.925	22.919	35.806	41.959

We can see from table 2.9 an increase of the degree of uniformity, except for the dimensional interval between 50 and 20 μm, due to the dimensional impurities

present in the sample, evident also in panel E of the figure 2.12. Another effect of washing is the homogenization of the curvature. From table 2.10 we see an increase of the diameters, especially for the Sauter diameter, according to the graphical results of the figure 2.12.

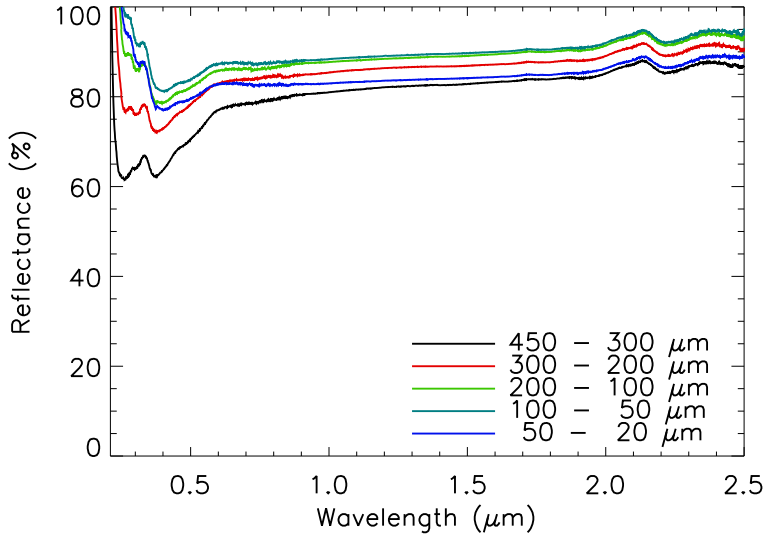

Figure 2.13: Spectra of the sample after the washing procedure.

Comparing the spectral results in the range between 0.2 and 2.5 μm (figure 2.8 and 2.13) we see an increase of the continuum level and of the separation between the different grain size curve.

Concerning the bands depth, comparing figure 2.9 and 2.14 we can see a similar trend for the band at 1.70 μm with just about 10 % offset. For the bands at 0.254 and 0.350 μm there is a different offset between finest (30 %) and the biggest grains (10 %) that increase the closing to a linear low.

Comparing the infrared range (1.7 $\div$ 25.0 μm, figure 2.10 and 2.15) we see an increase in the level of the continuum near the short wavelength according to the results obtained in the 0.2 $\div$ 2.5 μm range, but the minimum value of the band at 2.9 μm does not change. For the restrahlen bands we can see an increment of

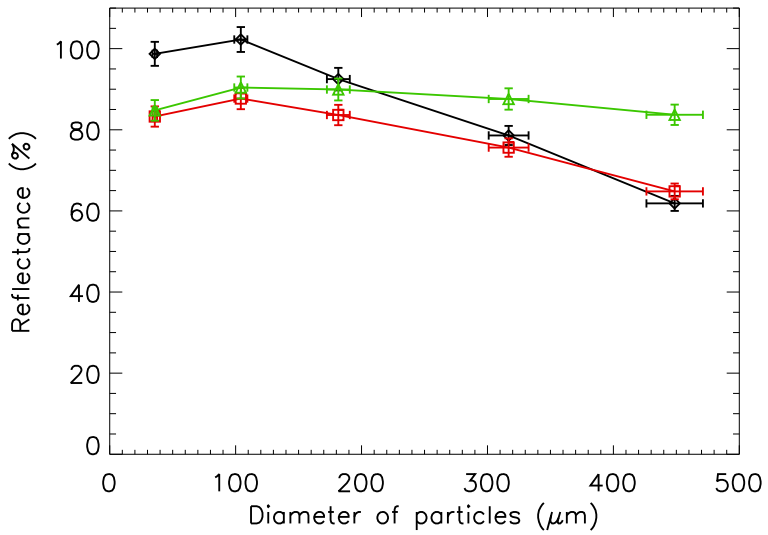

Figure 2.14: Level of the reflectance of the spectra at 0.254 μm (black line), at 0.350 μm (red line) and at 1.7 μm (green line) versus the grain size for the washed samples.

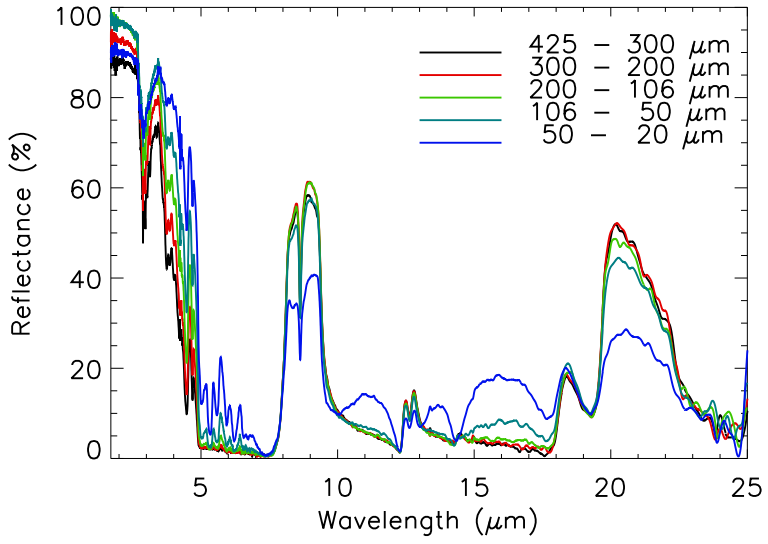

Figure 2.15: Spectra of the sample after the washing procedure.

about 20 % and the shape of the trend lines, comparing figure 2.16 with figure

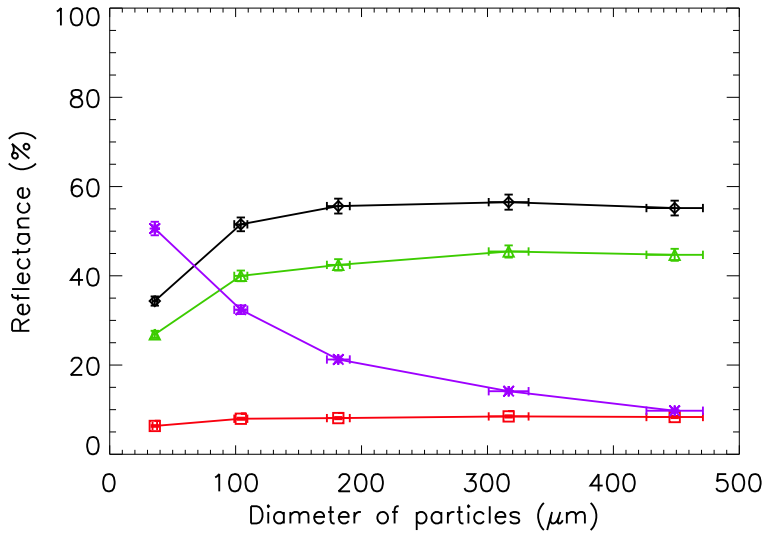

Figure 2.16: Level of the reflectance of the spectra at the restrahlen bands for the washed samples versus the grain size. In particular at 8.5 μm (black line), at 12.4 μm (red line) and at 21.0 μm (green line). For comparison the trend at 4.47 μm (violet line), corresponding to an absorption band, is also added.

2.11, has become more regular. Strangely the restrahlen band at 12.40 μ seems not influenced by the washing procedure in the general trend of the curve, but only in the size around 200 μm. Viceversa, for the absorption band, we can see a strong decrease in reflectance (15 %) for the small particles; such offset decreases with the increasing size of the grains.

The results show us that the influence of the size contamination is selective. In fact we can find bands not influenced, for example that at 2.9 μm, and bands strongly influenced, such as the 4.47 μm. For the level of the restrahlen bands we see a wide range of different variations, suggesting much caution in the use of such bands for the determination of the sample size.

Chapter 3

Intimate mixture

In this chapter I describe the theory of the intimate mixture, from Hapke's equations of intimate mixtures to laboratory simulations and remote sensing applications.

3.1 Hapke equations of intimate mixtures

Few materials found in nature consist of only one type of particles. Hence for the understanding of remote sensing measurement, it is necessary to be able to calculate the spectral behavior of mixture of different particle types. In remote sensing, two kinds of mixtures are of interest: areal and intimate.

3.1.1 Areal mixtures

Areal mixtures are also known as inhomogeneneous, linear, macroscopic and checkerboard mixtures. In an areal mixture, the surface viewed by the detector,

consists of several unresolved, smaller patches, each of which consists of a pure material. In this case the total reflectance is simply the linear sum of each reflectance weighted by the corresponding area. That is,

$$r = \sum_j F_j r_j. \tag{3.1}$$

Here r may represent any type of reflectance, as appropriate, r_j is the same type of reflectance for the jth component, and F_j is the fraction of the area viewed by the detector that is occupied by the jth component.

3.1.2 Intimate mixtures

Intimate mixtures are also called homogeneous and microscopic mixtures. In an intimate mixture the surface consists of different types of particles mixed homogeneously together in close proximity. In this case the averaging process is at the level of the individual particle, and the parameters appearing in the radiative transfer equation, are an average of the corresponding properties of the various type of particles present in the mixture, properly weighted by their cross-sectional area. Because the reflectance equation depends nonlinearly, by such parameters, the reflectance of an intimate mixture is a non linear function of the reflectance of the pure components, as it has been noted empirically by several authors (Nash & Conel, 1974; Cord *et al.* , 2002; Chemtob & Glotch, 2007).

The formula for intimate mixtures has another important use: calculating the effects on the reflectance of small asperities and subsurface fractures at the surface of grains. Such structures may be treated as small particles mixed with the larger ones. If the surface structures are smaller then the wavelength, they can act as Rayleigh

scatterers and absorbers. If the imaginary part of the refractive index is small, they act primarily as scatterers and increase the reflectance. However, if k is large, as for a metal, the asperities are efficient Rayleigh absorbers and lower the reflectance.

The mixing formula for each parameters follows from the definition of that parameter, as given in section 1.3. Because these formulas follow from the definition in the radiative-transfer equation, they are independent of the method or type of approximation used to solve that equation. Mixtures are often specified by the fractional mass of each component, rather then by the number of particles. Assuming that the particles are similar, the subscript j refers to any property of the particles, such as size, shape or composition. Then the *cross-sectional area* of the j^{th} type of particle is

$$\sigma_j = \pi a_j^2, \tag{3.2}$$

where a_j is the radius of the jth type of particle. The *bulk density* of the jth component is

$$\mathscr{M}_j = N_j \frac{4}{3} \pi a_j^3 \rho_j, \tag{3.3}$$

where N_j is the number of particles of type j per unit of volume, and ρ_j is their *solid density*. Then

$$N_j \sigma_j = \frac{3}{4} \frac{\mathscr{M}_j}{\rho_j a_j} = \frac{3}{2} \frac{\mathscr{M}_j}{\rho_j D_j}. \tag{3.4}$$

where $D_j = 2a_j$ is the equivalent size of the jth type of particle. From equation(1.25), (1.26) and (1.28), the average single scattering-albedo is

$$w_m = \frac{S}{E} = \frac{\sum_j N_j \sigma_j Q_{Sj}}{\sum_j N_j \sigma_j Q_{Ej}} = \left(\sum_j \frac{\mathscr{M}_j Q_{Sj}}{\rho_j D_j} \right) \Big/ \left(\sum_j \frac{\mathscr{M}_j Q_{Ej}}{\rho_j D_j} \right) \tag{3.5}$$

and the average particle scattering function is

$$p(g) = \frac{G(g)}{S} = \frac{\sum_j N_j \sigma_j Q_{Sj} p_j(g)}{\sum_j N_j \sigma_j Q_{Sj}} = \left(\sum_j \frac{\mathscr{M}_j Q_{Sj}}{\rho_j D_j} p_j(g) \right) \Big/ \left(\sum_j \frac{\mathscr{M}_j Q_{Sj}}{\rho_j D_j} \right). \quad (3.6)$$

Because $w_j = Q_{Sj}/Q_{Ej}$, the last two expression may be written in the alternative forms

$$w_m = \frac{\sum_j N_j \sigma_j Q_{Ej} w_j}{\sum_j N_j \sigma_j Q_{Ej}} = \left(\sum_j \frac{\mathscr{M}_j Q_{Ej}}{\rho_j D_j} w_j \right) \Big/ \left(\sum_j \frac{\mathscr{M}_j Q_{Ej}}{\rho_j D_j} \right) \quad (3.7)$$

$$p(g) = \frac{\sum_j N_j \sigma_j Q_{Ej} w_j p_j(g)}{\sum_j N_j \sigma_j Q_{Ej} w_j} =$$

$$= \left(\sum_j \frac{\mathscr{M}_j Q_{Ej}}{\rho_j D_j} w_j p_j(g) \right) \Big/ \left(\sum_j \frac{\mathscr{M}_j Q_{Ej}}{\rho_j D_j} w_j \right). \quad (3.8)$$

So we can write equation (1.44) as

$$r_h(i) = \frac{1 - \gamma_m}{1 + 2\gamma_m \mu_0}, \quad (3.9)$$

with $\gamma_m = \sqrt{1 - w_m}$.

3.2 Samples

For this study we will use calcite, quartz, already described in section 2.4, dolomite and gypsum mixed, in different ratios.

3.2.1 Calcite

The carbonate mineral calcite is a chemical or biochemical calcium carbonate corresponding to the formula $CaCO_3$ and is one of the most widely distributed

minerals on the Earth's surface. It is a common constituent of sedimentary rocks, limestone in particular. It is also the primary mineral in metamorphic marble. Moreover occurs as a mineral vein in deposits from hot springs, and also occurs in caverns as stalactites and stalagmites. Calcite is often the primary constituent of the shells of marine organisms, e.g., plankton (such as coccoliths and planktic foraminifera), the hard parts of red algae, some sponges, brachiopoda, echinoderms, most bryozoa, and parts of the shells of some bivalves, such as oysters and rudists). Calcite represents the stable form of calcium carbonate; aragonite will change to calcite at 470°C. Calcite crystals are hexagonal-rhombohedral, though actual calcite rhombohedrons are rare as natural crystals. However, they show a remarkable variety of habits including acute to obtuse rhombohedrons, tabular forms, prisms, or various scalenohedrons. Calcite exhibits several twinning types adding to the variety of observed forms. It may occur as fibrous, granular, lamellar, or compact. Cleavage is usually in three directions parallel to the rhombohedron form. Its fracture is conchoidal, but difficult to obtain.

It has a Mohs hardness of 3, a specific gravity of 2.71, and its luster is vitreous in crystallized varieties. Color is white or colorless, though shades of gray, red, yellow, green, blue, violet, brown, or even black can occur when the mineral is charged with impurities. Calcite is transparent to opaque and may occasionally show phosphorescence or fluorescence. It is perhaps best known because of its power to produce strong double refraction of light, such that objects viewed through a clear piece of calcite appear doubled in all of their parts.

At a wavelength of 590 nm calcite has ordinary and extraordinary refractive indices of 1.658 and 1.486, respectively (Roberts *et al.* , 1990). As for what concerns the spectral signature,, group theoretical analysis of the carbonate molecule predict four

normal modes listed in table 3.1.

Table 3.1: Normal modes of the CO_3^{-2} ion.

Mode[1]		Symmetry	Selection rules	Frequency[2]
ν_1	Symmetric stretch	A_1'	Raman	1064 cm^{-1}
ν_2	Out-of-plane bend	A_2''	IR	879 cm^{-1}
ν_3	Asymmetric stretch	E'	IR+ Raman	1415 cm^{-1}
ν_4	In-plane bend	E'	IR+Raman	680 cm^{-1}

[1]Labeling according to Herzberg (1945).
[2]Frequencies given by Farmer (1974).

3.2.2 Dolomite

Sedimentary carbonate rocks and minerals both composed of calcium magnesium magnesium carbonate $CaMg(CO_3)_2$ found in crystals belong to the Dolomite group. Dolomite rock (also known as dolostone) is composed predominantly of the mineral dolomite. Limestone that is partially replaced by dolomite is referred to as dolomitic limestone, or in old U.S. geologic literature as magnesian limestone. Dolomite was first described in 1791 as the rock by the French naturalist and geologist, Déodat Gratet de Dolomieu (1750-1801) for exposures in the Dolomite Alps of northern Italy. The mineral dolomite crystallizes in the trigonal - rhombohedral system. It forms white, gray to pink, commonly curved crystals, although it is usually massive. It has physical properties similar to those of the mineral calcite, but does not rapidly dissolve or effervesce (fizz) in dilute hydrochloric acid. The Mohs hardness is 3.5 to 4 and the specific gravity is 2.85. Refractive index values are $n_\omega = 1.679$ - 1.681 and $n_\varepsilon = 1.500$.

Table 3.2: Physical and optical property of dolomite.

Color	White, Gray, Reddish white, Brownish white, Gray
Crystal habit	Massive - Uniformly indistinguishable crystals forming large masses
Crystal system	Trigonal - Rhombohedral H-M Symbol ($\bar{3}$) Space Group: R $\bar{3}$
Twinning	common {110}
Cleavage	is perfect in three directions forming rhombohedrons
Fracture	Brittle - Conchoidal - Very brittle fracture producing small, conchoidal fragments
Mohs Scale	hardness 3.5-4
Luster	Vitreous (Glassy)
Refractive index	n_ω = 1.679 - 1.681, n_ε = 1.500
Optical Properties	2V(meas.) = Small
Pleochroism	Forms two series, with ankerite and with kutnohorite.
Streak	White
Specific gravity	2.85
Diaphaneity	translucent; may appear opaque in larger specimens

Crystal twinning is common. A solid solution series exists between dolomite and iron rich ankerite. Small amounts of iron in the structure give the crystals a yellow to brown tint. Manganese substitutes in the structure also up to about three percent MnO. A high manganese content gives the crystals a rosy pink color noted in the image above. A series with the manganese rich kutnohorite may exist. Lead and zinc also substitute in the structure for magnesium.

The frequencies of the spectral signatures of two significative members dolomite class are reported in table 3.3.

Table 3.3: Major spectral features of dolomite (Huang & Kerr, 1960).

Mineral	**Formula**	ν_1	ν_2	ν_3	ν_4
Ankerite	$Ca(Fe, Mg)(CO_3)_2$	-	877	1450	726

Table 3.3: Major spectral features of dolomite (Huang & Kerr, 1960)...(*continue*)

Mineral	**Formula**	ν_1	ν_2	ν_3	ν_4
Kutnahorite	$Ca(Mn,Mg)(CO_3)_2$	-	869	1435	721

3.2.3 Gypsum

Gypsum is a very soft mineral composed of calcium sulfate dihydrate, with the chemical formula $CaSO_4 \cdot 2H_2O$. Gypsum occurs in nature as flattened and often twinned crystals and transparent cleavable masses called selenite. It may also occur silky and fibrous, in which case it is commonly called satin spar. Finally it may also be granular or quite compact. In hand-sized samples, it can be anywhere from transparent to opaque. A very fine-grained white or lightly-tinted variety of gypsum is called alabaster, which is prized for ornamental work of various sorts. In arid areas, gypsum can occur in a flower-like form typically opaque with embedded sand grains called desert rose. In table 3.4 are shown the physical and optical properties of the gypsum (Roberts *et al.* , 1990).

Table 3.4: Physical and optical property of gypsum.

Color	White to grey, pinkish-red
Crystal habit	Massive, flat. Elongated and generally prismatic crystals
Crystal system	Monoclinic 2/m
Twinning	common {110}
Cleavage	2 good (66° and 114°)
Fracture	Conchoidal, sometimes fibrous
Mohs Scale	hardness 1.5-2
Luster	Vitreous to silky or pearly
Refractive index	α=1.520, β=1.523, γ=1.530
Optical Properties	2V = 58° +
Pleochroism	None
Streak	White
Specific gravity	2.31 - 2.33
Fusibility	3
Solubility	hot, dilute HCl
Diaphaneity	transparent to translucent

The frequencies of the spectral signatures of gypsum are listed in table 3.5, as reported by Hass, M. & Sutherland, G. B. B. M. (1956) and Moenke (1962).

Table 3.5: Major spectral features of gypsum.

Mode	**Frequency** (cm^{-1})
ν_1	1000 cm^{-1}
ν_2	-
ν_3	1131 cm^{-1}
ν_4	602 cm^{-1}

The gypsum, as shown by its chemical formula, is an hydrate salt. So, in addition to the vibrations of the group SO_4^{-2}, there are also the water vibrations, shifted by the presence of cations. The list of the vibration modes is reported in table 3.6, as

reported by Seidl *et al.* (1969).

Table 3.6: Vibrational frequencies of coordinated water influenced by cations and proton acceptor anions (IR, cm^{-1}).

Mode	**Frequency** (cm^{-1})
ν_3, ν_1	3549, 3496,3404,3242
ν_2	1681, 1618

3.3 Synthetic and theoretical mixtures

We define as *synthetic mixture* an intimate mixture made by mixing dust of mineral of well known characteristic (composition, diameter, spectral signature, etc.), in a well known ratio, and as *theoretical mixture* the result of equation (3.9), where the known properties of the components have been used as inputs.

In the following we will analyze several mixtures, of different components, ratio and grain size, in order to investigate the influence of each parameter. We start with a mixture, whose components have the same grain dimension, namely a mixture of quartz and calcite, in equal proportion in volume and grain size between 125 and 63 μm.

Table 3.7: Morphological parameters for the quartz and calcite with the nominal grain size between 125 and 63 μm.

Sample	$D[3,2](\mu m)$	$D[4,3](\mu m)$	Cu	Cc
SiO_2	103.98	122.32	1.89	0.97
$CaCO_3$	100.98	114.49	1.76	0.98

The results of laser diffraction analysis are reported in table 3.7 and in figures 3.1 and 3.2 according to the discussion given in section 2.1.

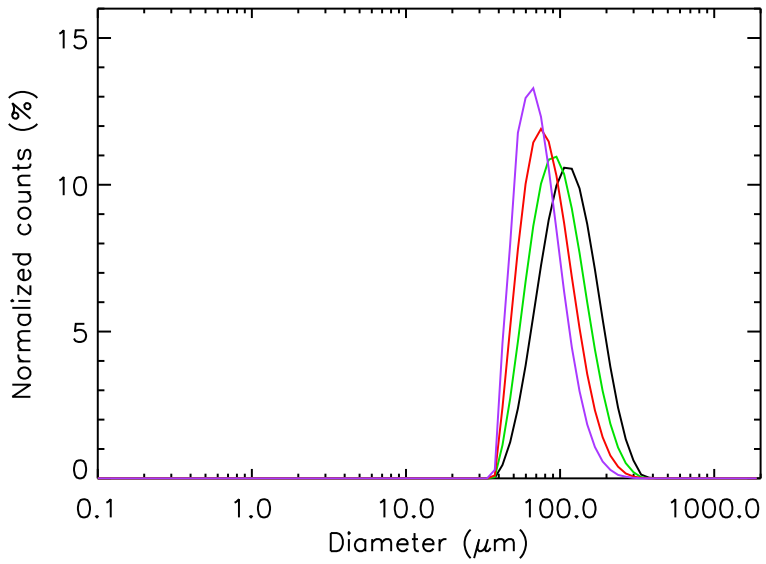

Figure 3.1: Plot of the normalized counts of quartz sample with a nominal grain size between 125 and 63 μm. The black line is the equivalent volume distribution, the green line is the equivalent surface distribution, the red line is the length equivalent distribution and the violet line is the number distribution.

For the spectral signature of the samples in the range between 1.7 and 25.0 μm we can refer to figures 3.3 and 3.4.

If we apply equations (1.44)[3] and (1.45) to the spectra shown in figures 3.3 and 3.4, we obtain directly the single scattering albedo for each wavelength, as reported in figures 3.5 and 3.6.

Using the data shown in figures 3.5 and 3.6 as input for equation (3.9), with the assumptions that $Q_{Ej} = 1$, all the incident radiation is either adsorbed or scattered, and density of minerals are $\rho_{quartz} = 2.62 \quad g/cm^3$ and $\rho_{calcite} = 2.71 \quad g/cm^3$, we obtain the reflectance shown in figure 3.7

[3]As we discussed in section 2.3.3 the instrument covering the range between 1.7 and 25.0 μm has an incidence angle i of 13°, and μ_0 is linked to i as described in (1.33).

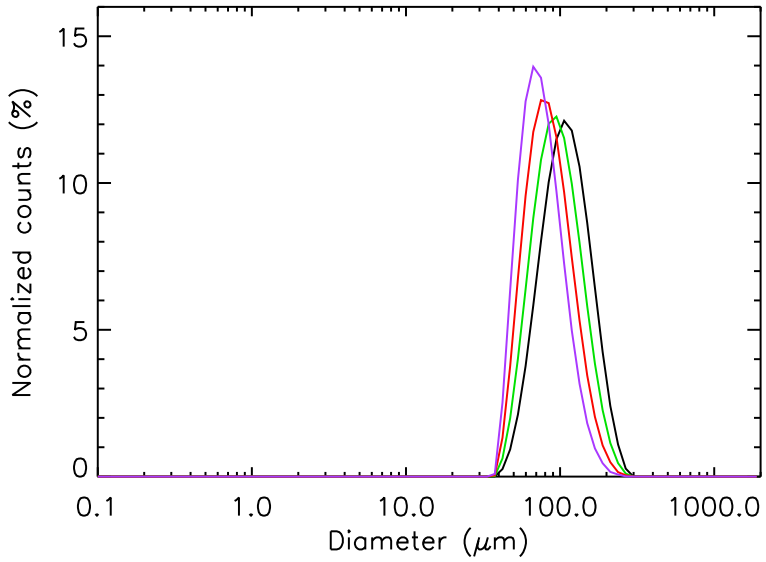

Figure 3.2: Plot of the normalized counts of calcite sample with a nominal grain size between 125 and 63 μm. The black line is the equivalent volume distribution, the green line is the equivalent surface distribution, the red line is the length equivalent distribution and the violet line is the number distribution.

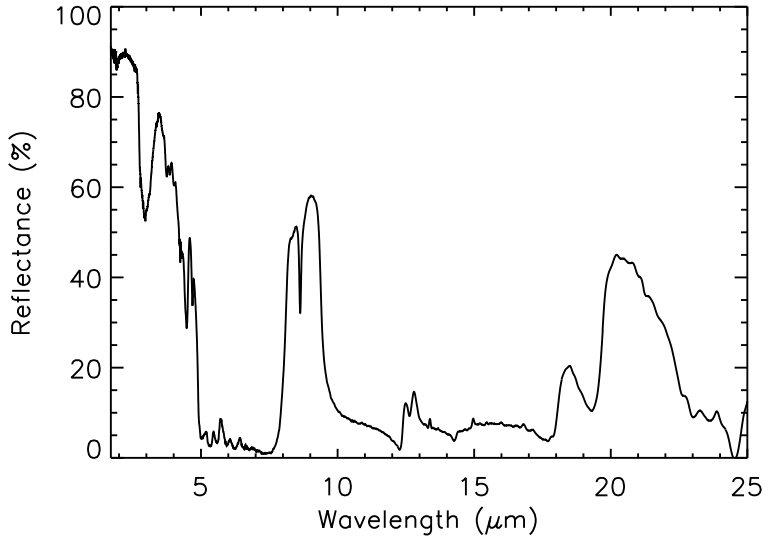

Figure 3.3: Spectrum of the quartz sample with grain size between 125 and 63 μm, in the range between 1.7 and 25.0 μm.

Figure 3.8 shows the spectrum of the corresponding synthetic mixture of calcite and quartz with ratio 0.5 in volume. In order to emphasize the difference between the synthetic and theoretical mixture, we plot both the spectra together in figure 3.9.

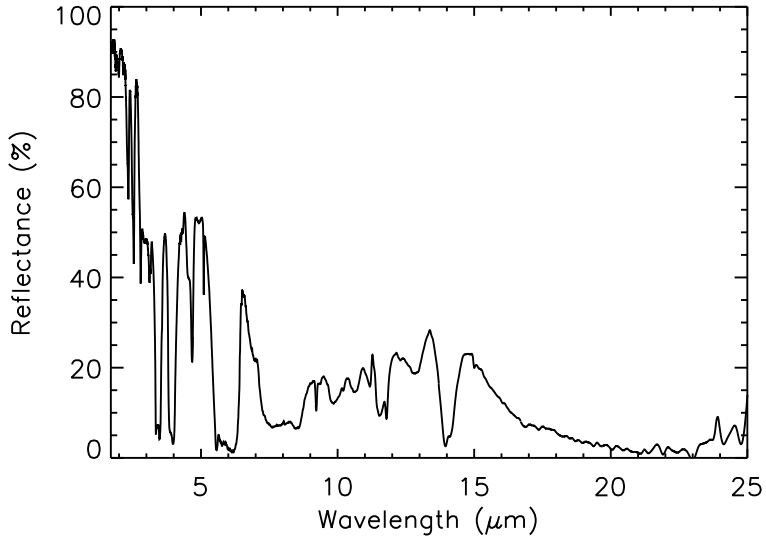

Figure 3.4: Spectrum of the calcite sample with grain size between 125 and 63 μm, in the range between 1.7 and 25.0 μm.

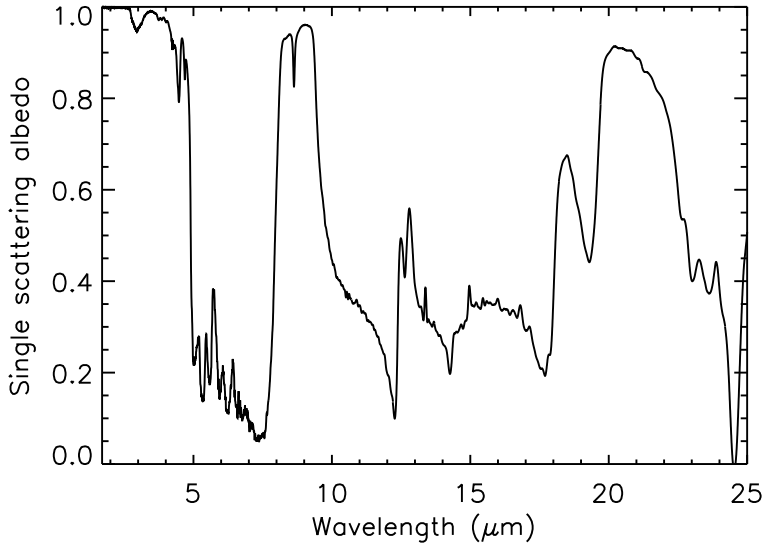

Figure 3.5: Single scattering albedo for the sample of quartz with grain size between 125 and 63 μm, in the range between 1.7 and 25.0 μm.

Analyzing the discrepancies between the two spectra, we notice that they are almost exclusively limited to the restrahlen bands of the two components, around 9 and 22 μm for quartz and 7 and 15 μm for calcite. Those discrepancies are probably linked to the nature of the restrahlen bands that are related to surface effects whereas the

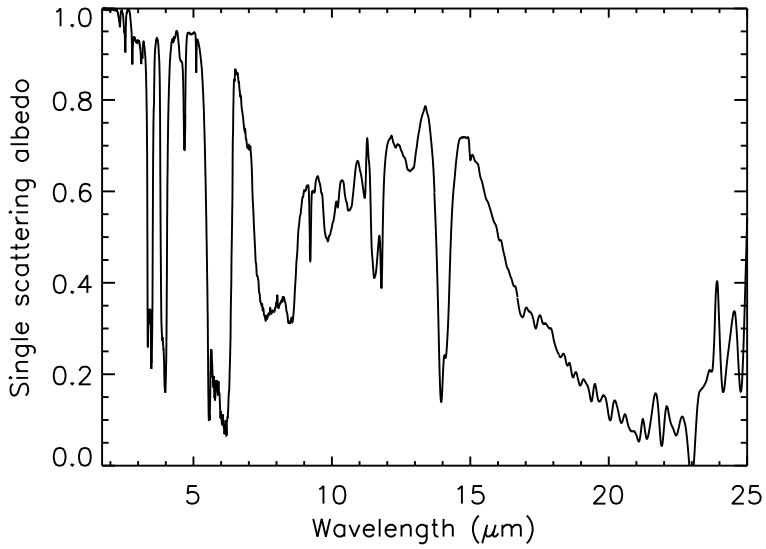

Figure 3.6: Single scattering albedo for the sample of calcite with grain size between 125 and 63 μm, in the range between 1.7 and 25.0 μm.

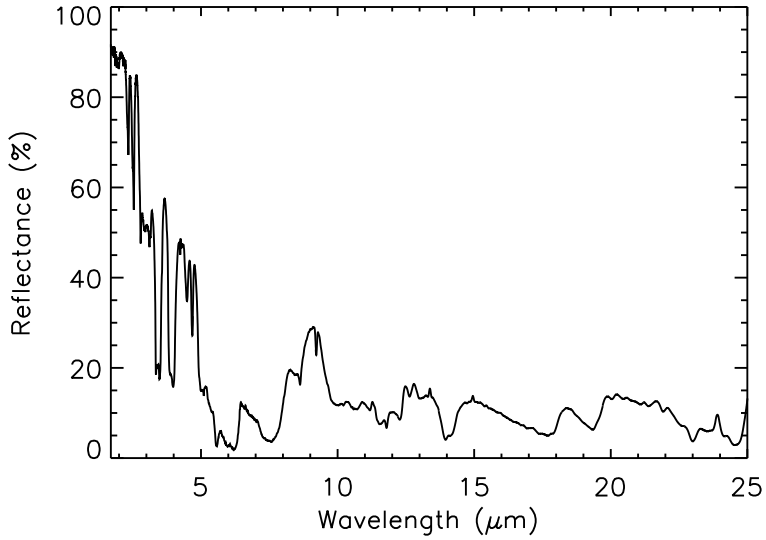

Figure 3.7: Spectrum of the theoretical mixture of quartz and calcite (ratio 0.5) with a grain size between 125 and 63 μm, in the range between 1.7 and 25.0 μm.

other feature are basically due to volume scattering. Thus it is possible that the values of the size used in the theoretical mixture are not fully representative of our samples in this spectral range.

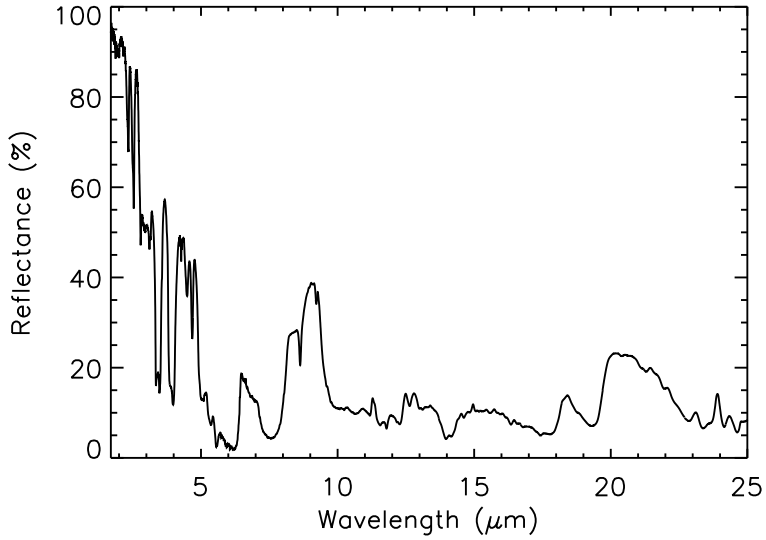

Figure 3.8: Spectrum of the synthetic mixture of quartz and calcite (ratio 0.5) with a grain size between 125 and 63 μm, in the range between 1.7 and 25.0 μm.

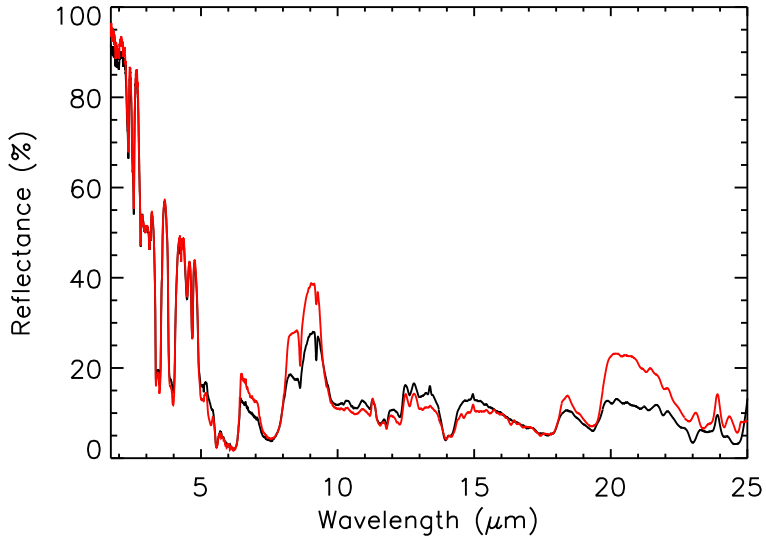

Figure 3.9: Comparison between the spectra of the theoretical, black line, and the synthetic mixture, red line, of quartz and calcite with a grain size size between 125 and 63 μm and a ratio of 0.5, in the range between 1.7 and 25.0 μm.

We then apply the same analysis to an equivalent mixture of dolomite and gypsum, whose size distributions are shown in figures 3.10 and 3.11 respectively, while their morphological parameters are listed in table 3.8.

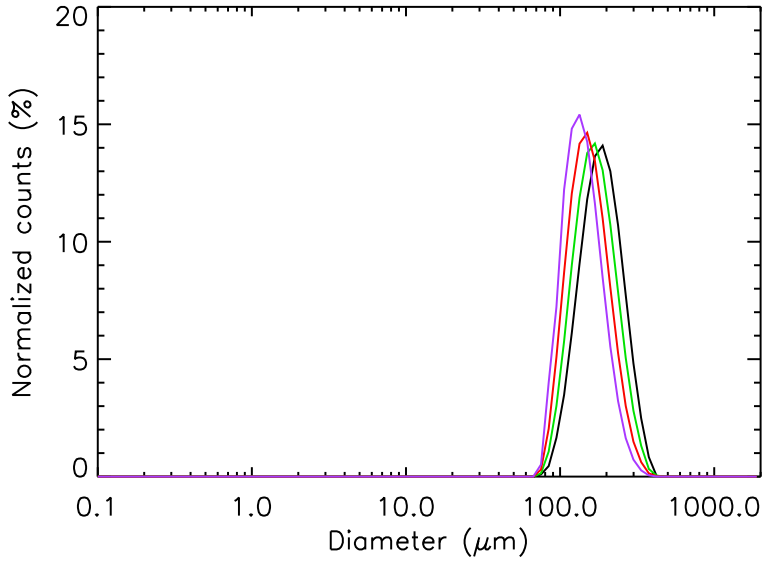

Figure 3.10: Plot of the normalized counts of dolomite with a nominal grain size between 200 and 100 μm. The black line is the equivalent volume distribution, the green line is the equivalent surface distribution, the red line is the equivalent length distribution and the violet line is the number distribution.

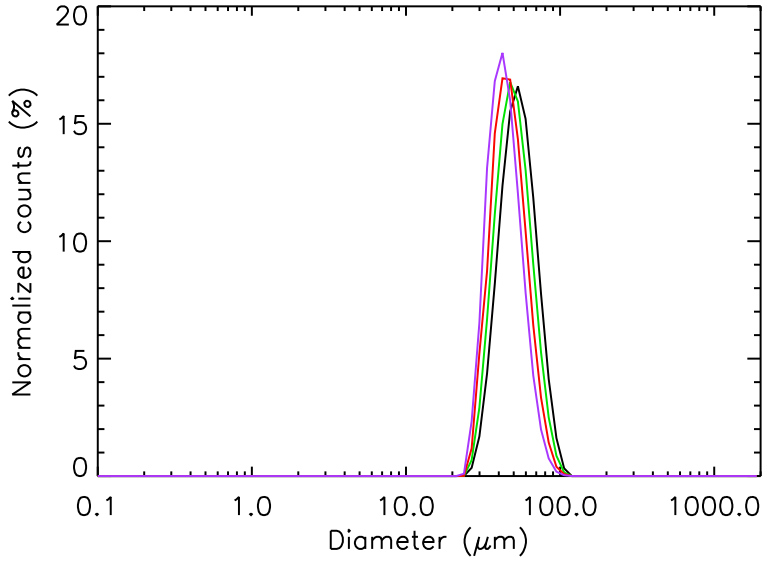

Figure 3.11: Plot of the normalized counts of gypsum with a nominal grain size between 200 and 100 μm. The black line is the equivalent volume distribution, the green line is the equivalent surface distribution, the red line is the equivalent length distribution and the violet line is the number distribution.

Table 3.8: Morphological parameters for the dolomite and gypsum with the nominal grain size between 200 and 100 μm.

Sample	$D[3,2](\mu m)$	$D[4,3](\mu m)$	Cu	Cc
$CaMg(CO_3)_2$	174.91	192.09	1.63	0.98
$CaSO_4 \cdot 2H_2O$	51.18	54.82	1.51	0.98

It is interesting to note that the figure shown in table 3.8 clearly evidences the difficult to precisely define the diameter of the grains. In fact, the values of $D[3,2]$ and $D[4,3]$ for gypsum particles are considerably smaller than the nominal range, 200 $\div$ 100 μm, due to the gypsum high hygroscopicity. This is because gypsum, during dry sieving, adsorbs environmental humidity and hence the grains cement to each other by hydrogen bonds. Such clusters are not able to cross the sieve meshes and look larger than their real size. On the other hand, in the laser diffractometer, using an appropriate dispersant (ethanol, CH_3CH_2OH) and ultrasonic shocks, we break the hydrogen bonds and measure the real grains diameter. Spectral measurement are affected both by the size of the cluster and by the size of the single grain.

The comparison, as shown in figure 3.12, between the theoretical and the synthetic mixture exhibit reduced discrepancies. As in the case of the mixture of quartz and calcite (figure 3.9), discrepancies are located in restrahlen bands, at 6.5 and 9 μm. The two spectra diverge in a significant way also beyond 16 μm, but in this range the reflectance level of the two component is really low and strongly affected by noise. However, since observed discrepancies are not larger then 4 %, which is at the edge of our spectrometer repeatability (about the 3 %), we can consider the match quite good. This can be due to an increased reliability in the derivation of the equivalent

diameters for the latter samples, as shown by the uniformity coefficients of tables 3.7 and 3.8.

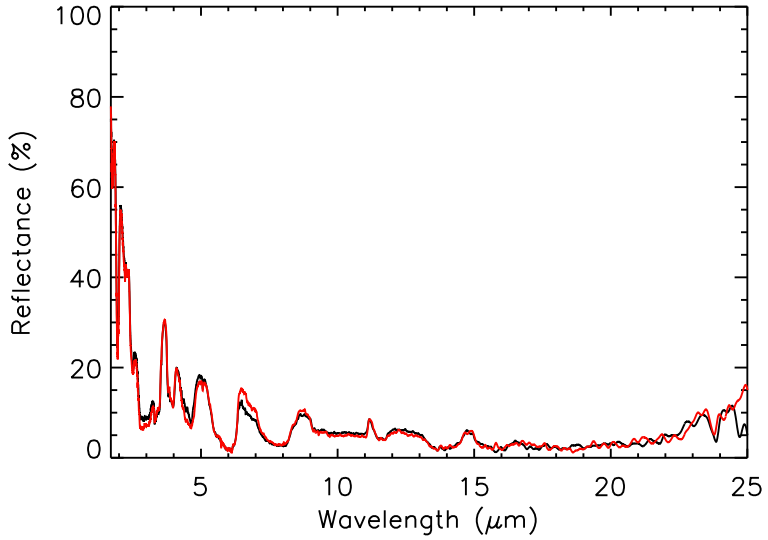

Figure 3.12: Comparison between the spectra of the theoretical, black line, and synthetic mixture, red line, of dolomite and gypsum with a grain size size between 200 and 100 μm and a ratio of 0.5, in the range between 1.7 and 25.0 μm.

From these two examples it is clear that, in this kind of application, it is also important to work with samples of high dimensional purity.

Chapter 4

Derivation of optical constants

In this chapter we discuss the importance of optical constants in the planetary research, in particular in the use of radiative transfer model. At the same time the methodology for the derivation of the optical constants from reflectance measurement will be another subject of this chapter.

4.1 Optical constants

In real materials, the polarization[1] does not respond instantaneously to an applied field. This causes dielectric loss, which can be expressed by permittivity[2] that is

[1]Polarization is the vector field that expresses the density of permanent or induced electric dipole moments in a dielectric material. The polarization vector $\mathcal{P}$ is defined as the dipole moment per unit volume. The SI unit of measure is coulombs per square meter.

[2]Permittivity is a physical quantity that describes how an electric field affects and is affected by a dielectric medium, and is determined by the ability of a material to polarize in response to the field, and thereby reduce the field inside the material. Thus, permittivity relates to a material's ability to transmit (or "permit") an electric field. The permittivity of a material is usually given relative to that of vacuum, as a relative permittivity ε_r (also called dielectric

both complex and frequency dependent. Real materials are not perfect insulators either (i.e. they have non-zero direct current conductivity). Taking both aspects into account, we can define a *complex index of refraction*:

$$\tilde{n} = n - \mathrm{i}k. \tag{4.1}$$

Where n is the *refractive index* indicating the phase velocity of electromagnetic wave in the material, given by the product $\sqrt{\varepsilon_r}\sqrt{\mu_{m0}}$, k is called the *extinction coefficient*, which indicates the amount of absorption loss when the electromagnetic wave propagates through the material. Both n and k depend on the frequency (wavelength).

The fact that n varies with frequency (except in vacuum, where all frequencies travel at the same speed, c) is known as dispersion, and it is what causes a prism to divide white light into its constituent spectral colors, explains rainbows, and is the cause of the chromatic aberration in lenses. In regions of the spectrum where the material does not absorb, the real part of the refractive index tends to increase with frequency. Near absorption peaks, the curve of the refractive index has a complex trend given by the Kramers-Krönig relations (Kronig, 1926; Kramers, 1927), and can decrease with frequency.

Since the refractive index of a material varies with the frequency of light, it is usual to specify the corresponding vacuum wavelength at which the refractive index is measured. Typically, this is done at various well-defined spectral emission lines; for example, n_D is the refractive index at the Fraunhofer D line, the center of the yellow

constant). The actual permittivity is then calculated by multiplying the relative permittivity by ε_0, the vacuum permittivity given by the ratio $1/c^2\mu_{m0}$,: $\varepsilon = \varepsilon_r\varepsilon_0 = (1 + \chi_e)\varepsilon_0$, where χ_e is the electric susceptibility of the material.

sodium double emission at 589.29 nm wavelength.

The Sellmeier equation (Zelmon *et al.* , 1997; Bruner *et al.* , 2003) is an empirical formula that works well in describing dispersion, and Sellmeier coefficients are often quoted instead of the refractive index in tables.

As mentioned above, dielectric losses and non-zero DC conductivity (Parkhutik & Shershulskii, 1986) cause absorption. Good dielectric materials such as glass have extremely low DC conductivity, and at low frequencies the dielectric loss is also negligible, resulting in almost no absorption ($k \approx 0$). However, at higher frequencies (such as visible light), dielectric loss may increase absorption significantly, reducing the material's transparency at these frequencies.

The real and imaginary parts of the complex refractive index are related through the Kramers-Krönig relations. For example, one can determine a material's full complex refractive index as a function of wavelength from an absorption spectrum of the material.

4.2 Methodology of derivation of optical constats

From a mathematical point of view, the basic problem in determining the real n and imaginary k parts of the index of refraction from given values of reflectance, transmittance or emissivity is that one must determine two functions from a given single relation. The problem has no solution, and one must therefore either obtain a second, independent spectrum or introduce some assumptions that makes n and k not independent of each other. There are two assumptions that are currently used. The first is that n and k are the real and imaginary part of a function $\tilde{n}(\nu)$, which is analytic in ν considered as a complex variable. This assumption

has been used to derive the Kramers-Krönig (hereinafter K-K) integral formula, which, in essence, supplies the needed independent spectrum (namely, the phase spectrum) that, together with the given amplitude spectrum, allows to find $n(\nu)$ and $k(\nu)$. According to the second assumption, based on the previously described theory of dispersion, the spectrum is due to a number of simple resonances (Lorentz oscillators). The basic procedure consists in measuring the sample spectrum and fitting, by successive iterations, the experimental spectrum to one calculated from a set of Lorentz oscillators. It is customary to rely on the least squares technique to find the best values of each oscillator parameters in order to overcome the effects of noise in the measured spectrum. A dispersive analysis has the advantage of representing the optical properties in a concise form (i.e. a table of Lorentz oscillator parameters and the defining equations are all that is required to define the optical properties at any desired frequency in the range of validity). On the contrary, other methods, such as K-K analysis, require extensive tables to adequately describe the optical properties. Moreover, the K-K procedure is not as good as dispersion analysis, especially if accurate values of the optical constants are desired in regions where $k < 0.1$ (Spitzer & Kleinman, 1961). For a more systematic description of the various technique for the derivation of the optical constants and the related formulae we refer to Marra (2005).

4.3 Derivation from Hapke reflectance equation

The Hapke equation of the directional-hemispherical reflectance (Hapke, 1981), with the approximation reported in section 1.3, is

$$r_h = \frac{1-\gamma}{1+2\gamma\mu_0}. \tag{4.2}$$

Deriving w from equation (4.2), we obtain:

$$w = 1 - \left(\frac{1-r_h}{1+2\mu_0 r_h}\right)^2. \tag{4.3}$$

If we suppose that for our sample, in the spectral region of interest, the *size parameter*, $X = \pi D/\lambda$, is greater than 1, we can describe the scattering efficiency (Q_S) with the equation:

$$Q_S = S_e + (1-S_e)(1-S_i)\left[(1-f)\frac{1}{e^{\alpha\langle\mathcal{D}\rangle} - S_i} + f\frac{1}{e^{\alpha\Delta\mathcal{D}} - S_i}\right], \tag{4.4}$$

where S_e refers to the radiation reflected by the external surface of each grain and S_i is related to the radiation transmitted inside the grain and reflected by its internal surface,

$$S_e = \frac{(n-1)^2 + k^2}{(n+1)^2 + k^2} + 0.05 \tag{4.5}$$

$$S_i = 1 - \frac{4}{n(n+1)^2}; \tag{4.6}$$

$$\alpha = \frac{4\pi k}{\lambda} \tag{4.7}$$

is the absorption coefficient, $\langle \mathcal{D} \rangle$ is the mean absorbtion path through the particles, $\Delta\mathcal{D}$ is the mean path associated with scattering by surface asperities or subsurface fractures and f is the fraction of light scattered by the particles.

If $X \gg 1$ (i.e. we are in the geometric-optics region) we can assume that the extinction efficiency, Q_E, is equal to 1 and since $w = Q_S/Q_E$, we obtain that $w = Q_S$; there is therefore a direct correlation between the experimental data and the optical constants. In this case the problem is to find the solution of an equation linking two variables, n and k, and three free parameters, $\mathcal{D}$, $\Delta\mathcal{D}$ and f, to the experimental measurement, r_h. From equations (4.7), (4.5) and (4.6) we can see that α, S_e and S_i depend only on λ, n and k, the variables the we wish to derive. Using geometrical consideration and assuming that only a small part of the light is scattered, $f \simeq 0.2$ (Hapke & Wells, 1981). We can assort that the mean absorption path, $\langle \mathcal{D} \rangle$, is of the order of the radius of the particles. In figure 4.1 geometrical considerations on the free space between grains are reported in order to evaluate the mean path associated to the scattering. If we suppose grains are well packed, examining the horizontal section (figure 4.1, panel A) we evaluate the maximum free space between grains, whose surface are represented by the arches, ad $D(\sqrt{2} - 1)$. In the vertical section (figure 4.1, panel B) we evaluate the maximum free space as $D(\sqrt{3} - 1)/2$. We estimate the mean path associated to the scattering between these two values.In such case, we can write Q_S only as a function of n, k and D.

4.4 Samples

To perform an experimental validation of the equations described above, we will compare the results obtained using a pair of real and a pair of synthetical samples.

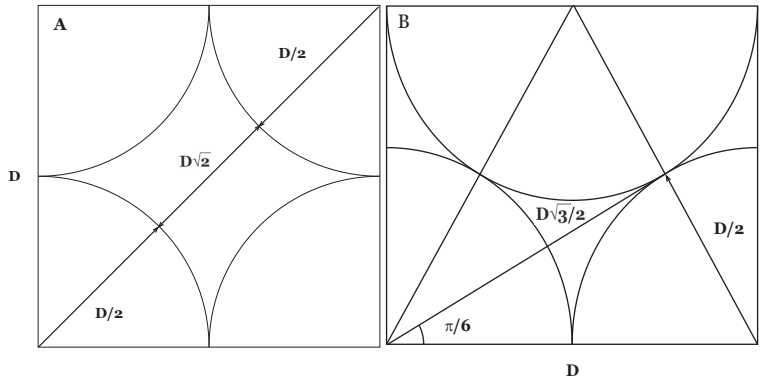

Figure 4.1: Geometrical considerations on the mean path associated to the scattering. In the two figures the horizontal (panel A) and vertical (panel B) section of well packed grains is shown.

The aim of this choice is to create a mixture of two samples of the same mineral, but of different size. For this test we used two consecutive dimensional classes of the same mineral. We derive independently the imaginary part of the optical constants, and the single scattering albedo from equation (4.4). For the comparison we use the mixtures laws discussed in section 3.1.

As real sample we will use washed quartz, described in the section 2.4, and in particular that with a grain size in the ranges 200 ÷ 106 μm and 106 ÷ 50 μm. In figure 4.2 we report the dimensional distribution of the two samples, and in table 4.1 the morphological parameters. In figure 4.3 is shown the dimensional distribution of the theoretical sample.

Table 4.1: Morphological parameter of two quartz samples.

Sample	$D[3,2]$	$D[4,3]$	Cu	Cc
200 ÷ 106 μm	174.941	197.273	1.738	0.980

Table 4.1: Morphological parameter of two quartz samples... (*continue*)

Sample	$D[3,2]$	$D[4,3]$	Cu	Cc
$106 \div 50$ μm	91.976	104.362	1.766	0.980

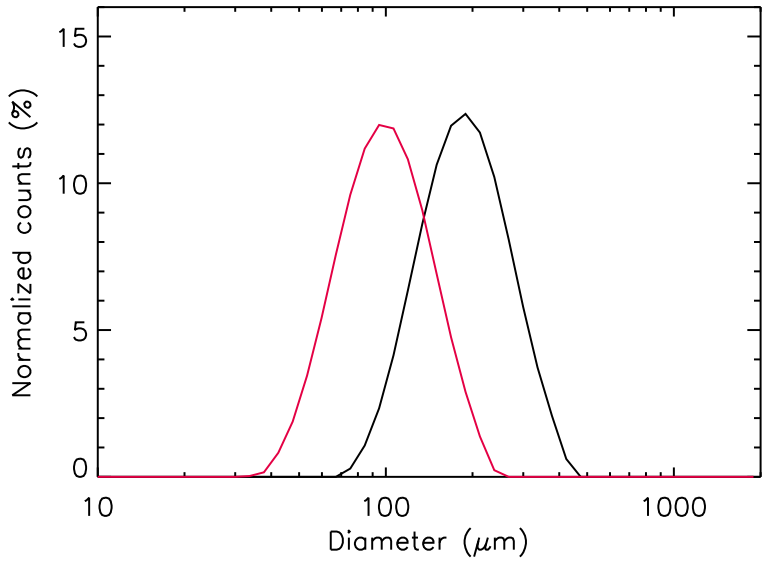

Figure 4.2: Dimensional distribution of the two samples of quartz; the black line is the sample with grain size in the range 200 ÷ 106 μm; the red line the sample with grain size between 106 ÷ 50 μm.

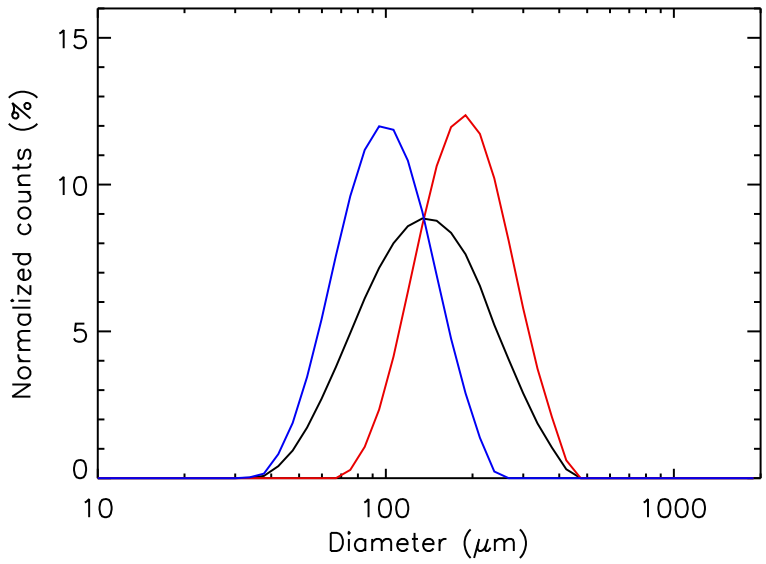

Figure 4.3: Grainsize distribution of the theoretical mixture, black line, and of the two components. The component with a dimension between 200 and 106 μm is represented by red line, the component between 106 and 50 μm by the blue line.

The morphological parameters are calculated using the definition given in section 2.1 and the distribution on figure 4.3. The results are shown in table 4.2. We report the percentile D_{50} instead of the diameter $D[4,3]$ because of the difficulties in obtaining the latter, and in force of the lower indetermination associated with the former.

Table 4.2: Morphological parameter of the theoretical sample.

D_{50}	Cu	Cc
126.61 ± 10.25	2.00	0.99

4.5 Results and discussion

For the two size classes, whose morphological and dimensional description was given in the previous section, we performed a measurement of directional-hemispherical reflectance, in the spectral range $0.2 \div 2.5$ μm, already reported in section 2.5 and reproduced in figure 4.4.

With those samples we are in the geometric-optics region, in fact, as shown in figure 4.5, both samples satisfy the condition $X \gg 1$, in the whole spectral range. We can therefore use the approximation given in equation (4.4) and derive the optical constants.

Using equation (4.3) we obtain the single-scattering albedos for the two samples, shown in figure 4.6

The application of equation (4.4) is based on the assumption that the real part of the optical constant, (n), is constant in the selected wavelength range, so that can be reduced to an equation in k with particle size as parameter. In order to simplify equation (4.4), we can approximate the exponential part by the second order of the

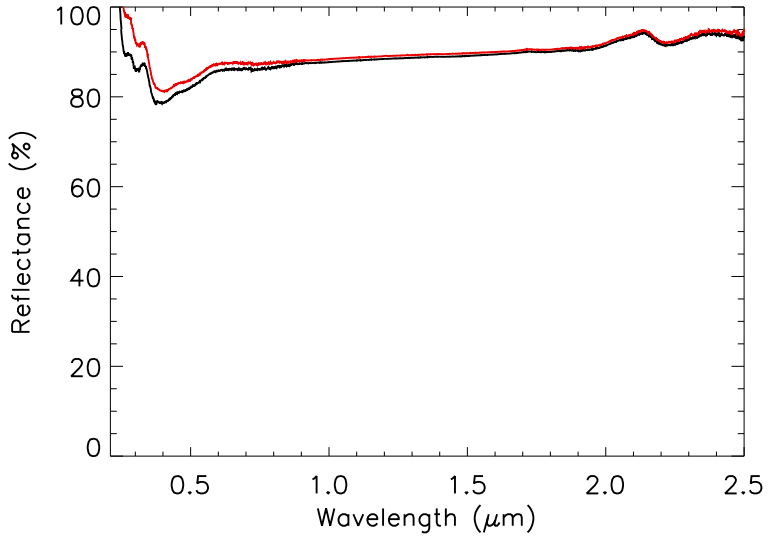

Figure 4.4: Reflectance spectra of the two quartz samples in the spectral range between 0.2 and 2.5 μm. The black line is associated to the sample with sieve size between 200 and 106 μm, the red line to the sample between 106 and 50 μm.

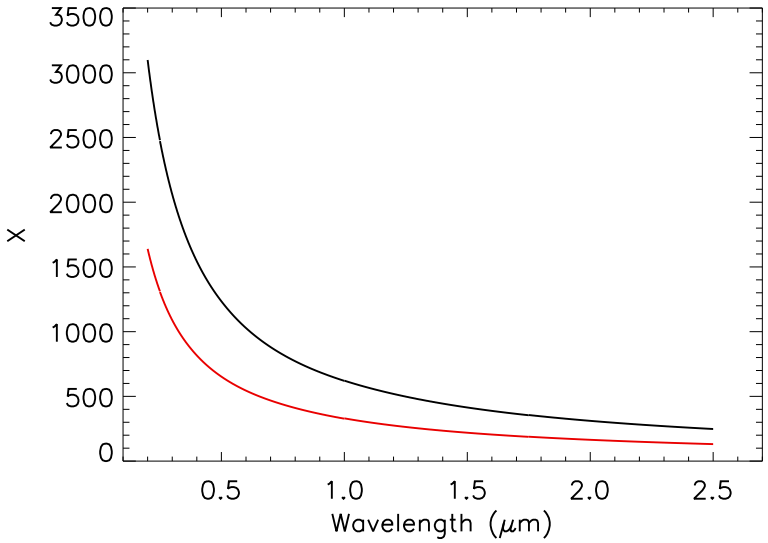

Figure 4.5: Size parameter versus wavelength in the spectral range between 0.2 and 2.5μm. The black line is related to the sample with dimensional range between 200 and 106 μm, the red line to the sample between 106 and 50 μm.

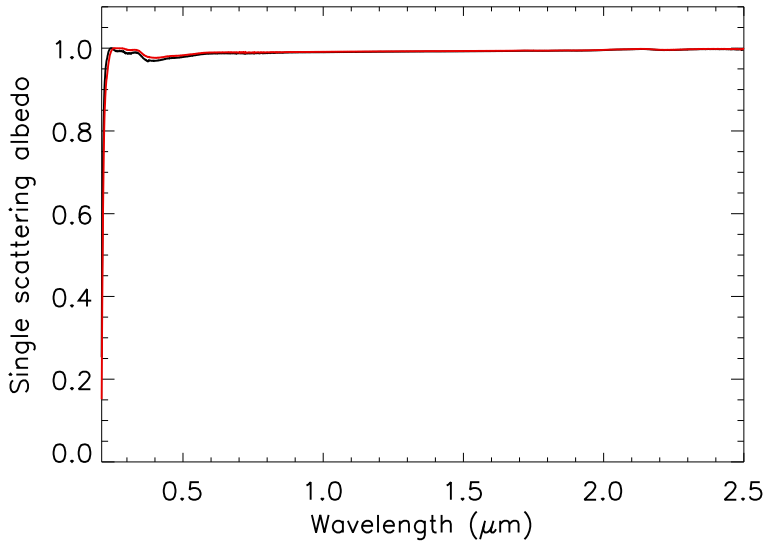

Figure 4.6: Plots of the albedos derived by equation (4.3) for the samples with sieve dimension between 200 ÷ 106 μm (black line) and 106 ÷ 50 μm (red line).

Mac Laurin expansion.

$$\frac{1}{e^{ax}-S_i} = \frac{1}{1-S_i} + x\left[\frac{ae^{ax}}{(e^{ax}-S_i)^2}\right]_{x=0} + \frac{x^2}{2}\left[\frac{2a^2e^{2ax}}{(e^{ax}-S_i)^3} - \frac{a^2e^{ax}}{(eax-S_i)^2}\right]_{x=0}$$

that can be written as

$$\frac{1}{e^{ax}-S_i} = \frac{1}{1-S_i} + x\left(\frac{a}{(1-S_i)^2}\right) + \frac{x^2}{2}\left(\frac{2a^2}{(1-S_i)^3} - \frac{a^2}{(1-S_i)^2}\right) \tag{4.8}$$

where a assume the values of either $4\pi\langle\mathcal{D}\rangle/\lambda$ or $4\pi\Delta\mathcal{D}/\lambda$. Table 4.3 reports the values of the parameters selected for the solution of equation 4.4, according to the discussion of section 4.3. The value of n reported in Table 4.3 is derived by Palik (1991). Taking into account the values reported in various handbooks and websites, we estimated that the average n value of the actual mineral we used should differ from the adopted value no more than 5% in the whole spectral range.

Table 4.3: Parameters used in the equation (4.4) for the determination of the values of k.

Parameters	200 ÷ 106 μm	106 ÷ 50 μm
n	1.57	1.57
$\langle \mathcal{D} \rangle$	95.80	52.20
$\Delta \mathcal{D}$	72.46	38.10
f	0.2	0.2

The results of the numeric procedure for the calculation of k are reported in figure 4.7, while the comparison between the values of albedo derived using the mixtures law (section 3.1) and those derived using the albedo obtained from equation (4.4) is reported in figure 4.8. As it can be seen, the agreement is good enough and it is rather difficult to distinguish between the two plots.

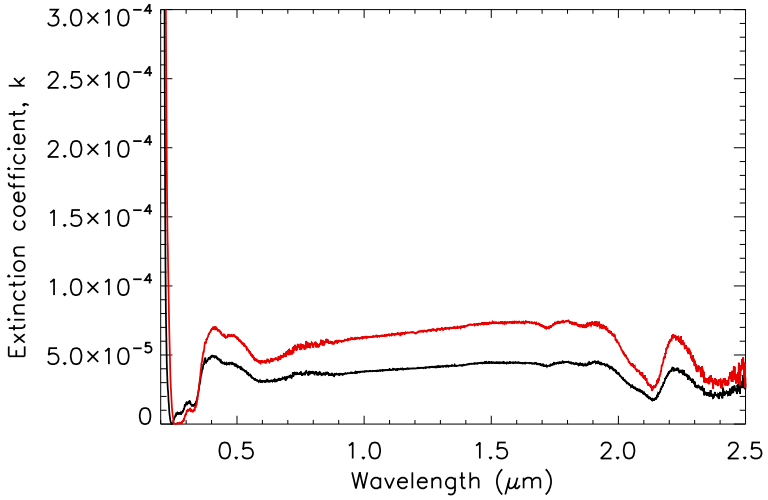

Figure 4.7: The extinction coefficients values, k, for the samples with dimension between 200 ÷ 106 μm (black line) and that with dimension between 106 ÷ 50 μm (red line).

It is quite difficult to assess the uncertainty on derived values of the imaginary part of

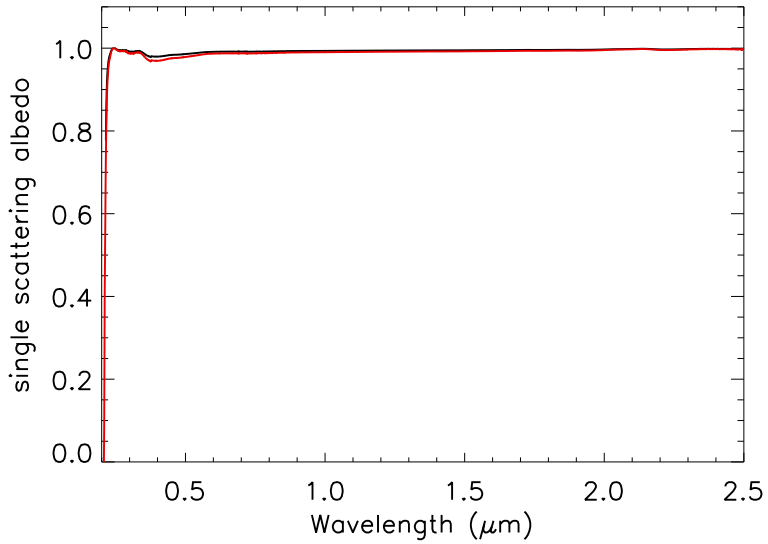

Figure 4.8: Comparison between the single scattering albedo derived using (4.4) with the albedo derived using the theoretical mixture.

the refractive index k, since it is due not only to the reproducibility of the reflectance spectra, but also to the complicated error propagation related to equations (4.4), (4.5) and (4.6). By taking into account the above considerations, we can estimate an upper limit of 10% on the whole wavelength range.

The results reported in figures 4.7 and 4.8 appear quite interesting, especially because they are obtained with a new and definitely no time consuming procedure. In literature there are also present data by Wenrich & Christensen (1996), by Parker *et al.* (1978) and by Lamy (1977), who determined the complex refractive index of quartz in the spectral ranges of mid infrared and far ultraviolet, respectively. Unfortunately a comparison cannot be done, since the above authors use very different experimental measurements as well as theoretical approaches, which are not sensitive to the low values of k we are able to reproduce, by limiting the spectral range between 0.2 and 2.5 μm only.

We are fully aware that the procedure described in this work has been used only in

a preliminary version. However, due to the encouraging results obtained so far, we are planning future improvements aimed to reduce of the degrees of freedom of the algorithm and develop of an independent checking technique. In the next future I plan to extend the applicative range of this procedure for the mid-infrared and this will be relevant, not only for obtaining optical constants in a more useful range, but also for comparison with the results obtained by other authors.

Conclusions

In this thesis I described the importance of obtaining the correct morphological parameter of a particulate sample, in order to model its spectral behavior for several applications.

In particular I illustred the difficulty to associate a correct size parameter (diameter) to each sample. In fact I introduced several diameters that, modeling those of real grains, emphasize different morphological properties (i.e. maximum length, surface, volume, etc.) and the related distributions. For a more effective analysis of this issue, I defined two parameters, useful for the evaluation of the distribution quality: the coefficient of uniformity (Cu) linked to the width of the distribution, and the coefficient of curvature (Cc) linked to the shape of distribution. I emphasized how the continuum level, especially in the visible range, and the spectral contrast are linked to morphological parameters. Plotting these quantities versus the grain size, allows to see that, when Cu and Cc assume optimal values (i.e. after the washing procedure), they show a regular trend.

I applied Hapke's theory for an intimate mixture, describing its remote sensing applications and also, in this case, I stressed the role of uniformity and curvature

coefficients. The intimate mixture equations, in fact, link the single scattering albedos of components and of mixtures, weighting them proportionally to the grains diameter. This link emphasizes the effect of not selecting the "right" diameter, especially in the restrahlen bands, where reflectance increases quickly (see figure 3.9) and discrepancies are more often seen. The very small differences between the theoretical and experimental spectra in the second mixture (see figure 3.12), suggest that the obtained results are quite reliable. This reliability needs obviously further checks on a large range of samples for mixtures with two or more components.

In addition, I described a methodology for deriving the optical constants in the spectral range between 0.5 and 2.5 μm, alternative to the classical methods and I explained how it is possible to obtain the extinction coefficients using the single scattering albedos calculated in chapter 3. Finally I described a comparison of the results of these calculations with the results obtained for the intimate mixture, clearly evidencing the limits due to the high number of assumptions.

Appendix A

Udden-Wentworth classification

In table we report the complete classification of sediment basing on size of particles as reported by Wenthworth (1922)

Dimension	**Name**
>256 mm	boulders
256÷128 mm	large cobbles
128÷64 mm	small cobbles
64÷32 mm	very coarse gravel
32÷16 mm	coarse gravel
16÷8 mm	medium gravel
8÷4 mm	fine gravel
4÷2 mm	very fine gravel
2÷1 mm	very coarse sand

Dimension	Name
1÷0.5 mm	coarse sand
0.5÷0.25 mm	medium sand
0.25÷0.125 mm	fine sand
0.125÷0.062 mm	very fine sand
0.062÷0.031 mm	coarse silt
0.031÷0.016 mm	medium silt
0.016÷0.008 mm	fine silt
0.008÷0.004 mm	very fine silt
<0.004 mm	clay

Appendix B

Reflectance reference

B.1 Spectralon

Spectralon is a thermoplastic resin giving the highest diffuse reflectance of any known material or coating over the UV-VIS-NIR region of the spectrum. It can be machined into a wide variety of shapes for the construction of optical components. The material has a hardness roughly equal to that of high-density polyethylene and is thermally stable at over 350° C. It is chemically inert to everithing including the most powerful bases such as sodium amide and organo-sodium or lithium compounds. The material is extremely hydrophobic. Gross contamination of the material or marring of the optical surface can be remedied by sanding under a stream of running water. This surface refinishing both restores the original topography of the surface and returns the material to its original reflectance. Weathering tests on the material show no damage upon exposure to atmospheric UV flux. The material shows no

sign of optical or physical degradation after long-term immersion in sea water. The reflactance is generally > 99 % over the range from 0.4 to 1.5 μm and > 95 % from 0.25 to 2.50 μm. Surface or subsurface contamination may lower the reflectance at the extreme upper and lower ends of the spectral range. The material is also highly lambertian at wavelengths from 0.257 μm to 10.6 μm, although it exhibits a much lower reflectance at 10.6 μm, due to absorbance by the resin (Erb, 1975).

B.2 Infragold

Infragold is an electrochemically plated, diffuse, gold-metallic coating which exhibits excellent reflectance properties over the wavelength range from 0.7 to 20 μm. Infragold has excellent vacuum stability, with no outgassing reported. Laser damage threshold is approximately 19.3 J/cm^2 at 10.6 μm using CO_2 laser. This is considered above average for a plated surface. The threshold will increase if the material is cooled on exposure to laser, as in water-cooled integrating spheres or targets. The typical reflectance of Infragold is > 94 % above 1000 nm and data can be found at the National Institute of Standards and Technology (NIST). Infragold can be applied to metal parts, generally aluminum, nickel or steel, although it has been applied with success to copper and tungsten. It is generally used for reflectance integrating spheres and accessories for NIR to MIR applications and is suitable for many space applications (Budde, 1959; Erb, 1975).

Appendix C

List of simbols

a	mean particle radius
A	area
c	speed of light
C_c	coefficient of curvature, $(C_c = D_{30}^2)/(D_{10} * D_{60})$
C_u	coefficient of uniformity, $C_u = D_{60}/D_{10}$
d	diameter
$\langle \mathcal{D} \rangle$	mean ray path through particle
$D[3,2]$	diameter of Sauter, $D[3,2] = \sum d^3 / \sum d^2$
$D[4,3]$	diameter of De Brouckere or volume moment mean, $D[4,3] = \sum d^4 / \sum d^3$
D_{xx}	percentile xx
$E(s, \Omega)$	volume extinction coefficient
e	zenith angle of emergence

$F(s,\Omega)$	volume emission coefficient
$F_S(s,\Omega)$	stimulated emission volume coefficient
$F_T(s,\Omega)$	thermal emission volume coefficient
$\mathcal{F}(z,\Omega)$	source function
$G(s,\Omega,\Omega')$	volume angular scattering
$H(x)$	Chandrasekhar function
i	zenith angle of incidence
i	$\sqrt{-1}$
I	radiance
J	irradiance
k	imaginary part of refractive index or extinction coefficient
$K(s,\Omega)$	volume absorption coefficient
$\mathscr{M}$	number
N	number of particles per unit volume
N_E	effective number of particles per unit volume
n	real part of refractive index
$\tilde{n}$	complex index of refraction
$\mathcal{P}$	polarization vector
$p(z,\Omega',\Omega)$	volume phase function
P_E	extinguished power
P_F	emitted power
P_S	scattered power
Q_A	absorption efficiency
Q_E	extinction efficiency

Q_S	scattering efficiency
r	bidirectional reflectance
r_h	directional-hemispherical reflectance
s	distance, position, line element
$S(s, \Omega)$	volume scattering coefficient
S_e	total Fresnel reflectivity for externally incidence light
S_i	total Fresnel reflectivity for internally incidence light
$\mathcal{V}$	volume
$w(z)$	volume single-scattering albedo
X	size parameter
Z	average distance between particles, $Z = N^{-1/3}$
α	absorption coefficient
χ_e	electric susceptibility
λ	wavelength
Δ	increment
ε	permittivity
ε_0	permittivity of vacuum
ε_r	relative permittivity or dielectric constant
μ	$\mu = \cos e$
μ_{m0}	magnetic permeability of vacuum
μ_0	$\mu_0 = \cos i$
θ	scatter angle
τ	optical depth
ϕ	filling factor
γ	albedo factor, $\gamma = \sqrt{1 - w}$

σ	particle cross-sectional area ($\sigma = \pi a^2$)
σ_A	particle absorption cross section
σ_E	particle extinction cross section
σ_S	particle scattering cross section
Ω	direction
ϑ	angle

Bibliography

Alderliesten, M. 1991. Mean Particle Diameters. Part II: Standardization of nomenclature. *Part. Part. Syst. Charact.*, **8**, 237–241.

Allen, T. 1999. *Particle size measurement*. London: Chapman and Hall.

Bandfield, J. L., Glotch, T. D., & Christensen, P. R. 2003. Spectroscopic identification of carbonate minerals in the Martian dust. *Science*, **301**, 1084–1087.

Bibring, J.-P., Langevin, Y., Gendrin, A., Gondet, B., Poulet, F., Berthé, M., Soufflot, A., Arvidson, R., Mangold, N., Mustard, J., & Drossart, P. 2005. Mars Surface Diversity as Revealed by the OMEGA/Mars Express Observations. *Science*, **307**, 1576–1581.

Bohren, C.F., & Huffman, D.R. 1983. *Absorption and scattering of light by small particles*. New York: John Wiley & Sons.

Bruner, A., Eger, D., Oron, M.B., Blau, P., Katz, M., & Ruschin, S. 2003. Temperature-dependent Sellmeier equation for the refractive index of stoichiometric lithium tantalate. *Optics Letters*, **28**, 194–196.

Budde, W. 1959. Standards of Reflectance. *J. Opt. Soc. Am.*, **50**, 217–220.

Burns, R. G. 1970. *Mineralogical Applications of Crystal Field Theory.* New York: Cambridge Univ. Press.

Cabrol, N. A., & Grin, E. A. 1999. Distribution, Classification, and Ages of Martian Impact Crater Lakes. *Icarus*, **142**, 160–172.

Chandrasekhar, S. 1960. *Radiative transfer.* New York: Dover.

Chapman, J. F., & Wardle, M. 2006. Dust grain dynamics in C-type shock waves in molecular clouds. *Mon. Not. R. Astron. Soc.*, **371**, 513–529.

Chemtob, S. M., & Glotch, T. D. 2007. Linear Deconvolution of Attenuated Total Reflectance Infrared Spectra of Fine-grained Mineral Mixtures. *Pages 1097–1098 of: Lunar and Planetary Institute Conference Abstracts.*

Christensen, P. R., Anderson, D. L., Chase, S. C., Clancy, R. T., Clark, R. N., Conrath, B. J., Kieffer, H. H., Kuzmin, R. O., Malin, M. C., Pearl, J. C., Roush, T. L., & Smith, M. D. 1998. Results from the Mars Global Surveyor Thermal Emission Spectrometer. *Science*, **279**, 1692–1698.

Christensen, P. R., Bandfield, J. L., Smith, M. D., Hamilton, V. E., & Clark, R. N. 2000. Identification of a basaltic component on the Martian surface from Thermal Emission Spectrometer data. *J. Geophys. Res.*, **105**, 9609–9622.

Christensen, P. R., McSween, H. Y., Bandfield, J. L., Ruff, S. W., Rogers, A. D., Hamilton, V. E., Gorelick, N., Wyatt, M. B., Jakosky, B. M., Kieffer, H. H., Malin, M. C., & Moersch, J. E. 2005. Evidence for magmatic evolution and diversity on Mars from infrared observations. *Nature*, **436**, 504–509.

Colman, S. M. 1986. *Rates of Chemical Weathering of Rocks and Minerals*. Orlando, Florida: Academic Press.

Cord, A., Pinet, P., Daydou, Y., & Chevrel, S. 2002. Influence of Linear Versus Non-linear Mixture On Bidirectional Reflectance Spectra With Simulated Geologic Targets. *EGS XXVII General Assembly, Nice, 21-26 April 2002, abstract #1295*, **27**, 1295.

Erb, W. 1975. Requirements for reflection standards and the measurement of their reflection values. *Appl. Opt.*, **14**, 493–499.

Farmer, V. C. 1974. *Infrared spectra of minerals*. London: Mineralogical Society.

Fonti, S., Jurewicz, A., Blanco, A., Blecka, M. I., & Orofino, V. 2001. Presence and detection of carbonates on the Martian surface. *J. Geophys. Res.*, **106**, 27815–27822.

Forget, F., & Pierrehumbert, R. T. 1997. Warming Early Mars with Carbon Dioxide Clouds That Scatter Infrared Radiation. *Science*, **278**, 1273–1276.

Gabas, N., Hiquily, N., & Laguérie, C. 1994. Response of Laser Diffraction Particle Sizer to Anisometric Particles. *Part. Part. Syst. Charact.*, **11**, 121–126.

Goldspiel, J. M., & Squyres, S. W. 1991. Ancient aqueous sedimentation on Mars. *Icarus*, **89**, 392–410.

Grassi, D., & Formisano, V. 2000. IRIS Mariner 9 data revisited: Aerosol dust composition. *Planet. Space Sci.*, **48**, 577–598.

Hapke, B. 1981. Bidirectional reflectance spectroscopy. 1. Theory. *J. Geophys. Res.*, **86**, 3039–3054.

Hapke, B. 1993. *Theory of reflectance and emittance spectroscopy.* Topics in Remote Sensing, Cambridge University Press, Cambridge, UK.

Hapke, B., & Wells, E. 1981. Bidirectional reflectance spectroscopy. II - Experiments and observations. *J. Geophys. Res.*, **86**, 3055–3060.

Hass, M., & Sutherland, G. B. B. M. 1956. The Infra-Red Spectrum and Crystal Structure of Gypsum. *Proceedings of the Royal Society of London. Series A, Mathematical and Physical Sciences*, **236**, 427–445.

Herzberg, G. 1945. *Molecular spectra and molecular structure. Vol.2: Infrared and Raman spectra of polyatomic molecules.* New York: Van Nostrand, Reinhold.

Hoefen, T. M., Clark, R. N., Bandfield, J. L., Smith, M. D., Pearl, J. C., & Christensen, P. R. 2003. Discovery of Olivine in the Nili Fossae region of Mars. *Science*, **302**, 627–630.

Huang, CK, & Kerr, PF. 1960. Infrared study of the carbonate minerals. *American Mineralogist*, **45**, 311–324.

Jakosky, B. M., Mellon, M. T., Kieffer, H. H., Christensen, P. R., Varnes, E. S., & Lee, S. W. 2000. The thermal inertia of Mars from the Mars Global Surveyor Thermal Emission Spectrometer. *J. Geophys. Res.*, **105**, 9643–9652.

Kerker, M. 1969. *The scattering of light and other electromagnetic radiation.* New York: Academic.

Kramers, H.A. 1927. La diffusion de la lumiere par les atomes. *Atti. Congr. Int. Fis. Como*, **2**, 545–557.

Kronig, R.D.L. 1926. On the theory of dispersion of x'rays. *J. Opt. Soc. Am.*, **12**, 547.

Lamy, P. L. 1977. Optical constants of crystalline and fused quartz in the far ultraviolet. *Appl. Opt.*, **16**, 2212–2214.

Lellouch, E., Encrenaz, T., de Graauw, T., Erard, S., Morris, P., Crovisier, J., Feuchtgruber, H., Girard, T., & Burgdorf, M. 2000. The 2.4-45 μm spectrum of Mars observed with the Infrared Space Observatory. *Planet. and Space Sci.*, **48**, 1393–1405.

Malin, M. C., & Carr, M. H. 1999. Groundwater formation of Martian valleys. *Nature*, **397**, 589–591.

Marra, A.C. 2005. *Spectral Properties of Particulate Materials of Martian Interest*. Ph.D. thesis, Università Degli Studi di Lecce.

Marzo, G. A., Blanco, A., De Carlo, F., D'Elia, M., Fonti, S., Marra, A. C., Orofino, V., & Politi, R. 2004. The optical constants of gypsum particles as analog of Martian sulfates. *Advances in Space Research*, **33**, 2246–2251.

Masursky, H., Boyce, J. M., Dial, A. L., Schaber, G. G., & Strobell, M. E. 1977. Classification and time of formation of Martian channels based on Viking data. *J. Geophys. Res.*, **82**, 4016–4038.

Maturilli, A., Helbert, J., Witzke, A., & Moroz, L. 2006. Emissivity measurements of analogue materials for the interpretation of data from PFS on Mars Express and MERTIS on Bepi-Colombo. *Planet. Space Sci.*, **54**, 1057–1064.

McKay, C. P., & Stoker, C. R. 1989. The Early Environment and its Evolution on Mars: Implications for Life. *Reviews of Geophysics*, **27**, 189–214.

McKay, D. S., Gibson, E. K., Thomas-Keprta, K. L., Vali, H., Romanek, C. S., Clemett, S. J., Chiller, X. D. F., Maechling, C. R., & Zare, R. N. 1996. Search for past life on Mars: Possible relic biogenic activity in martian meteorite ALH84001. *Science*, **273**, 924–930.

Moenke, H. 1962. *Mineralspektren.* Berlin: Akademie Verlag.

Mustard, J. F., Poulet, F., Head, J. W., Mangold, N., & Bibring, J. P. 2005a. Ancient Crust, Hydrolytic Weathering, and Impact Melt Preserved in the Isidis Basin, Mars. *AGU Fall Meeting Abstracts*, A–01.

Mustard, J. F., Poulet, F., Gendrin, A., Bibring, J.-P., Langevin, Y., Gondet, B., Mangold, N., Bellucci, G., & Altieri, F. 2005b. Olivine and Pyroxene Diversity in the Crust of Mars. *Science*, **307**, 1594–1597.

Nash, D., & Conel, J. 1974. Spectral reflectance systematics for mixture of powdered hypersthene, labradorite and ilmenite. *J. Geophys. Res.*, **79**, 1615–1621.

Nozawa, T., Kozasa, T., & Habe, A. 2006. Dust Destruction in the High-Velocity Shocks Driven by Supernovae in the Early Universe. *Astrophys. J.*, **648**, 435–451.

Orofino, V., Blanco, A., Fonti, S., Proce, R., & Rotundi, A. 1998. The infrared optical constants of limestone particles and implications for the search of carbonates on Mars. *Planet. Space Sci.*, **46**, 1659–1669.

Orofino, V., Blanco, A., Blecka, M. I., Fonti, S., & Jurewicz, A. 2000. Carbonates and coated particles on Mars. *Planet. Space Sci.*, **48**, 1341–1347.

Orofino, V., Blanco, A., Fonti, S., Marra, A. C., & Polimeno, N. 2002. The complex refractive index of limestone particles: an extension to the FIR range for Mars applications. *Planet. Space Sci.*, **50**, 839–847.

Palik, E.D. 1985. *Handbook of Optical Constants of Solids*. New York: Academic Press.

Palik, E.D. 1991. *Handbook of Optical Constants of Solids II*. New York: Academic Press.

Parker, T. J., Ford, J. E., & Chambers, W. G. 1978. The optical constants of pure fused quartz in the far-infrared. *Infrared Physics*, **18**, 215–219.

Parkhutik, VP, & Shershulskii, VI. 1986. Modelling of d. c. conductivity of thin disordered dielectrics. *Journal of Physics D. Applied Physics*, **19**, 623–641.

Pollack, J. B., Kasting, J. F., Richardson, S. M., & Poliakoff, K. 1987. The case of a wet, warm climate on Mars. *Icarus*, **71**, 203–224.

Pollack, J. B., Roush, T., Whitteborn, F., Bregman, J., Wooden, D., Stoker, C., Toon, O. B., Rank, D., Dalton, B., & Freedman, R. 1990. Thermal emission spectra of Mars (5.4-10.5 μm): Evidence for sulfates, carbonates, and hydrates. *J. Geophys. Res.*, **95**, 14595–14628.

Poulet, F., Mangold, N., Bibring, J., Loizeau, D., Mustard, J. F., Head, J. W., Gendrin, A., Ansan, V., Gomez, C., Masson, P., Neukum, & Omega-HRSC Co-I Teams, G. 2005. Evidence for Phyllosilicates in the Early Mars Crust at Nili Fossae and Mawrth Valles Using OMEGA and HRSC Data. *AGU Fall Meeting Abstracts*, B144.

Ran, D. 1998. Laser diffraction measurement. *Pages 201–208 of:* Ye, S. (ed), *Proc. SPIE Vol. 3558, p. 201-208, Automated Optical Inspection for Industry: Theory, Technology, and Applications II.*

Reichman, J. 1973. Determination of absorption and scattering coefficients for nonhomogeneous media. 1: Theory. *Appl. Opt.*, **12**, 1811–1823.

Roberts, W. L., Campbell, T. J., & Rapp Jr., G. R. 1990. *Encyclopaedia of Minerals.* New York: Chapman & Hall.

Salisbury, J. W., Walter, L. S., & Vergo, N. 1987. *Mid-infrared (2.1-25μm) Spectra of Minerals: First Edition.* U.S.G.S. Open-File Rept. U.S.G.S.

Seidl, V., Knop, O., & Falk, M. 1969. Infrared studies of water in crystalline hydrates: gypsum, $CaSO_4 \cdot 2H_2O$. *Canadian Journal of Chemistry*, **47**(8), 1361–1368.

Spitzer, W. G., & Kleinman, D. A. 1961. Infrared Lattice Bands of Quartz. *Physical Review*, **121**, 1324–1335.

van de Hulst, H.C. 1957. *Light scattering by small particles.* New York: John Wiley & Sons.

Wenrich, M. L., & Christensen, P. R. 1996. Optical constants of minerals derived from emission spectroscopy: Application to quartz. *J. Geophys. Res.*, **101**, 15921–15931.

Wenthworth, C. K. 1922. A scale of grade and clast terms for clastic sediments. *J. Geol.*, **30**, 377–392.

Williams, R. M. E., & Phillips, R. J. 2001. Morphometric measurements of martian valley networks from Mars Orbiter Laser Altimeter (MOLA) data. *J. Geophys. Res.*, **106**, 23737–23752.

Yung, Y. L., Nair, H., & Gerstell, M. F. 1997. CO_2 Greenhouse in the Early Martian Atmosphere: SO_2 Inhibits Condensation. *Icarus*, **130**, 222–224.

Zelmon, D.E., Small, D.L., & Jundt, D. 1997. Infrared corrected Sellmeier coefficients for congruently grown lithium niobate and 5 mol. magnesium oxide doped lithium niobate. *J. Opt. Soc. Am. B*, **14**, 3319–3322.

Zhou, Y., Li, D., Wang, L., Özkan, N., Chen, X. D., & Mao, Z. 2006. Influence of microemulsion cross-linking reaction and ball-milling on particle size characteristics of potato and maize starches. *International Journal of Food Engineering*, **2**, Iss. 4, Article 6.

Author Bibliography

Publications in International Journals

S. Fonti, G. Arnold, A. Blanco, L. Colangeli, M. D′Elia, F. De Carlo, S. Erard,F. Esposito, V. Formisano, A. C. Marra, G.A. Marzo, V. Orofino, E. Palomba,G. Piccioni, N. Polimeno and R. Politi *Laboratory measurements in support of the spectroscopy experiments on board the Mars express mission* Recent Research Developments in Astronomy & Astrophysics Vol. 1 (2003) Part I

G. Bellucci, F. Altieri, M. Blecka, R. Bonsignori, P. Coppo, S. Fonti, G. Marzo, S. Meli J. J. L. Moreno, B. Moshkin, G. G. Ori, V. Orofino, R. Politi, G. Preti, A. Romoli, T. Roush, B. Saggin, M. Sgavetti, D. Stam and L. Zasova *Infrared spectroscopy of Mars for exobiology applications* Recent Research Developments in Astronomy & Astrophysics Vol. 1 (2003) Part II

G. A. Marzo, A. Blanco, F. De Carlo, M. D′Elia, S. Fonti, A. C. Marra, V. Orofino, **R. Politi** *The Optical Constants of Gypsum Particles as Analog of Martian Sulphates* Advances in Space Research, Volume 33, Issue 12, 2004, Pages 2246-

2251.

Marra A.C., Politi R., Blanco A., Brunetto R., Fonti S., Marzo G.A., Orofino V. O*ptical Constants of Particulate Minerals from Reflectance Measurements: the Case of Calcite* J. Quant. Spectrosc. Ra., 100 250-255, 2006

Orofino V.; Politi R.; Blanco A.; Fonti S. *Diffuse reflectance of altered olivine grains: Remote sensing detection and implications for Mars studies*, Planetary and Space Science, Volume 54, Issue 8, p. 784-793, 2006

Conference Presentations and Proceedings

Fonti S., Blanco A., Cabrol N., De Carlo F., Grin E., Leone G., Marzo G. A., Orofino V., Politi R. *The Spectroscopic Investigation of the Martian Surface: a Combined Laboratory and Field Approach* Abstracts of Conference Papers of International Workshop: "Exploring Mars Surface and Its Terrestrial Analogues", Tozeur, Tunisia, 2001

Blanco A., Orofino V., Fonti S., De Carlo F., Marra A. C., Marzo G. A., Politi R. *Laboratory Studies of Carbonates and Martian Aerosol* Proceedings of the meeting: "Solids and molecules in space - I", S. Miniato, Italy, 2001.

Blanco A., Fonti S., Orofino V., De Carlo F., D′Elia M., Marra A. C., Marzo G. A., Politi R. *Laboratory Studies of Carbonates in Support to Mars Exploration* Proceedings of the meeting: "Quarto Convegno Nazionale di Scienze Planetarie", Bormio, Italy, 20 - 26 Gennaio 2002.

Marra A.C., Blanco A., De Carlo F., Fonti S., Marzo G.A., Orofino V., **Politi R.** *Spectroscopic measurements of Martian analog materials of paleoclimatic*

interest in Exploring Mars Surface and its Earth Analogues, Sicily and Mount Etna, 23-25 September 2002.

S. Fonti, A. Blanco, F. De Carlo, I. Longhi, A.C. Marra, G.A. Marzo, S. Meli, V. Orofino, R. Politi, M. Sgavetti *A combined laboratory and field approach for the spectroscopic investigation of Martian surface* in Exploring Mars Surface and its Earth Analogues, Sicily and Mount Etna, 23-25 September 2002.

M. D′Elia, A. Blanco, F. De Carlo, S. Fonti, A.C. Marra, G.A. Marzo, V. Orofino, R. Politi *Electron Microscopy In Support of Laboratory Measurements For the Mars Express Space Mission* Proceedings of the 6th Multinational Congress on Microscopy - European Extension, June 1-5, 2003, Pula, Croatia. Ed.: Ognjen Milat and Davor Ježek. Published by Croatian Society for Electron Microscopy, Frankopanska 1/dvor, Zagreb, Croatia, p. 454 - 455.

M. D′Elia, A. Blanco, F. De Carlo, S. Fonti, A.C. Marra, G.A. Marzo, V. Orofino, R. Politi *La Microscopia Elettronica come supporto alle misure di laboratorio effettuate per la missione spaziale Mars Express* LXXXVIII Congresso Nazionale Società Italiana di Fisica, Alghero, 119, 2002.

Politi R., Blanco A., De Carlo F., Fonti S., Marra A. C., Marzo G. A., Orofino V. *Spectroscopic Measure of Olivine Weathered by Acqueous Alteration* LXXXVIII Congresso Nazionale Società Italiana di Fisica, Alghero, 119, 2002.

S. Fonti, G. Arnold, A Blanco, G. Bonello, L. Colangeli, M. D'Elia, F. De Carlo, S. Erard, F. Esposito, V. Formisano, A. C. Marra, G. A. Marzo, V. Orofino, E. Palomba, G. Piccioni, R. Politi, C. Wagner *A Coordinated Laboratory Program in Support of the Spectroscopic Experiments on Board*

Martian Missions Submitted Mars Infrared Spectroscopy: From Theory and Laboratory to Field Observations, Houston, USA, June 4-6 2002

Politi, R.; Blanco, A.; De Carlo, F.; Fonti, S.; Marra, A.C.; Marzo, G.A.; Orofino, V. *Hemispherical reflectance of olivine samples weathered by acqueous alteration.* Poster at XXVII General Assembly of EGS , Nice, France 21 - 26 April 2002, EGS02-A-02461

De Carlo, F.; Blecka, M.; D'Elia, M.; Fonti, S.; Marzo, G.; Politi, R. *Laboratory and numerical simulations of Martian hematite spectra* 34th COSPAR Scientific Assembly, The Second World Space Congress, held 10-19 October, 2002 in Houston, TX, USA., p.2255

R. Politi, G. A. Marzo, A. Blanco, F. De Carlo, S. Fonti, A. C. Marra, V. Orofino *Spectroscopic search for fossils in terrestrial layered rocks* Second European Workshop on Exo/Astrobiology, Graz, Austria, 2002

M. D′Elia, A. Blanco, F. De Carlo, S. Fonti, A.C. Marra, G.A. Marzo, V. Orofino, R. Politi *Study and Characterization of Minerals in Planetary Science Usign Scanning Electron Microscopy* Proceedings of the meeting: "Quinto Convegno Nazionale di Scienze Planetarie", 15 - 20 September 2003, Gallipoli, Italy

R. Politi, G.A. Marzo, A. Blanco, S. Fonti and V. Orofino *Identification of Microfossils Features as Martian Analogs via Spectroscopic Analysis* Proceedings of the meeting: "Quinto Convegno Nazionale di Scienze Planetarie", 15 - 20 September 2003, Gallipoli, Italy

Politi R., Marzo G.A., Blanco A., Fonti S., Orofino V. *Searching for spectral signatures of fossils: Modelling and applications* III European Workshop on

Exo/Astrobiology, Madrid, Spain, 2004

Orofino V., Blanco A., D'Elia M., De Carlo F., Fonti S., Marra, A. C., Marzo G. A., Politi R., Verrienti C. *Spectroscopic studies of materials relevant for the hydrological evolution of Mars* Memorie della Societa Astronomica Italiana Supplement 6 76, 2005

Fonti, S.; De Carlo, F.; Marzo, G. A.; Altieri, F.; Blanco, A.; Dinoi, A.; Marra, A. C.; Orofino, V.; Politi, R.; Verrienti, C. *A radiative transfer model applied to the analysis of dust suspended in the martian atmosphere*, Second workshop on Mars atmosphere modelling and observations, held February 2 7 - March 3, 2006 Granada, Spain. Edited by F. Forget, M.A. Lopez-Valverde, M.C. Desjean, J.P. Huot, F. Lefevre, S. Lebonnois, S.R. Lewis, E. Millour, P.L. Read and R.J. Wilson. Publisher : LMD, IAA, AOPP, CNES, ESA, 2006., p.225

Politi R., Fonti S., Altieri F., Bellucci G., Bibring J.-P., Marzo G.A., *Martian iron silicates as water marker: mineralogical and grain size distribution*, Asia Oceania Geosciences Society 3rd Annual Meeting 10-14 July 2006, Singapore

Politi R., Marzo G.A., Blanco A., Brunetto R., D'Elia M., Dinoi A., Fonti S., Marra A.C., Orofino V., Verrienti C. *Planets seen by AstroLe*, Asia Oceania Geosciences Society 3rd Annual Meeting 10-14 July 2006, Singapore

Marzo, G. A.; Bellucci, G.; Fonti, S.; Saggin, B.; Alberti, E.; Altieri, F.; Politi, R.; Zasova, L.; The Mima Team, *MIMA: Mars Infrared MApper - The Fourier spectrometer for the ESA Pasteur/ExoMars rover mission*, Asia Oceania Geosciences Society 3rd Annual Meeting 10-14 July 2006, Singapore

Marzo G.A., Roush T. L., Fonti S., Politi R., *Cluster Analysis of the Circum-Chryse Region, Mars: Evidence for Cabonate Minerals*, Asia Oceania Geosciences Society 3rd Annual Meeting 10-14 July 2006, Singapore

Politi R., Marzo G.A., Blanco A., Brunetto R., D'Elia M., Dinoi A., Fonti S., Marra A.C., Orofino V., Verrienti C. *Planets seen by AstroLe*, 36th COSPAR Scientific Assembly. Held 16 - 23 July 2006, in Beijing, China., p.1228

Marzo, G. A.; Roush, T. L.; Fonti, S.; Formisano, V.; Politi, R.; Orofino, V.; Dinoi, A. *Cluster Analysis of PFS data: surface and aerosol mineralogy*, 36th COSPAR Scientific Assembly. Held 16 - 23 July 2006, in Beijing, China., p.1229

Marzo, G. A.; Bellucci, G.; Fonti, S.; Saggin, B.; Alberti, E.; Altieri, F.; Politi, R.; Zasova, L.; The Mima Team, *MIMA: Mars Infrared MApper - The Fourier spectrometer for the ESA Pasteur/ExoMars rover mission*, 36th COSPAR Scientific Assembly. Held 16 - 23 July 2006, in Beijing, China., p.1245

Politi, R.; Marzo, G. A.; Bonaccorsi, R.; Fonti, S.; Blanco, A.; Brunetto, R.; Marra, A. C., *Recognition of microfossils in rock matrix using Infrared and Raman Spectroscopy: a potential for Biosignatures Detection* 36th COSPAR Scientific Assembly. Held 16 - 23 July 2006, in Beijing, China., p.1268

Acknowledgements

I would like to express my gratitude to all those who helped me by material works and backing. In particular my thanks go to my tutor Sergio Fonti who proved to be champion of patience, supporting me in this not easy path. I am very thankful to Armando Blanco, Vincenzo Orofino and Francesco Strafella for suggestions often eye-opening.

My thanks go also to Marcella D'Elia and Luigi "Gino" Villa, whose support goes from help in fundamental measurements to more practical questions (without the demineralized water obtained by Gino no dimensional measurement could be possible).

The second price for patience goes to my friend Giuseppe A. Marzo whose friendship was demonstrated in many corners of the world. I warmly thanks the sacrificial victims of "Pandomime"[1] *Davide Elia and Achille A. Nucita and to the gentle side of the laboratory Loretta Campeggio, Berlinda Maiolo, Anna Cinzia Marra and Sarah Montanaro.*

Thanks go also to my friends Daniela, Giorgia, Antonio and Enzo; they helped me

[1] Is defined "pandomima" the eternal sunshine of my spotless mind.

to keep my feet on the ground when my mind went to stars. One special mention to Danilo and Ciccio, fellows of life in the few past years.

A great thank goes to my family whose support was and will be fundamental in this case as well as in other ones.

Last but not least my thanks goes to the woman in whose love I found the strength.

List of Figures

List of Tables